nature biomedical engineering

Article

https://doi.org/10.1038/s41551-024-01253-z

# Virally delivered CMYA5 enhances the assembly of cardiac dyads

Received: 12 July 2023

Accepted: 9 August 2024

Published online: 5 September 2024

Check for updates

Fujian Lu[1,2] ✉, Carter Liou[2], Qing Ma[2], Zexuan Wu[2,3], Bingqing Xue[4], Yu Xia[4], Shutao Xia[4], Michael A. Trembley[2], Anna Ponek[2], Wenjun Xie[5], Kevin Shani[6], Raul H. Bortolin[2], Maksymilian Prondzynski[2], Paul Berkson[2], Xiaoran Zhang[2], Francisco J. Naya[7], Kenneth C. Bedi[8], Kenneth B. Margulies[8], Donghui Zhang[4], Kevin K. Parker[6] & William T. Pu[2,9] ✉

Cardiomyocytes derived from human induced pluripotent stem cells (hiPSC-CMs) lack nanoscale structures essential for efficient excitation–contraction coupling. Such nanostructures, known as dyads, are frequently disrupted in heart failure. Here we show that the reduced expression of cardiomyopathy-associated 5 (CMYA5), a master protein that establishes dyads, contributes to dyad disorganization in heart failure and to impaired dyad assembly in hiPSC-CMs, and that a miniaturized form of CMYA5 suitable for delivery via an adeno-associated virus substantially improved dyad architecture and normalized cardiac function under pressure overload. In hiPSC-CMs, the miniaturized form of CMYA5 increased contractile forces, improved $Ca^{2+}$ handling and enhanced the alignment of sarcomere Z-lines with ryanodine receptor 2, a protein that mediates the sarcoplasmic release of stored $Ca^{2+}$. Our findings clarify the mechanisms responsible for impaired dyad structure in diseased cardiomyocytes, and suggest strategies for promoting dyad assembly and stability in heart disease and during the derivation of hiPSC-CMs.

In mature cardiomyocytes, cardiac dyads tightly couple electrical activity with $Ca^{2+}$ release and cardiomyocyte contraction. Dyads are nanoscopic $Ca^{2+}$ signalling structures formed by the close apposition of T-tubules (cell-wide, regularly distributed tubular invaginations of the plasma membrane that penetrate the cardiomyocyte interior)[1] with the junctional sarcoplasmic reticulum (jSR) (specialized regions of the SR enriched for the $Ca^{2+}$ release channel RYR2)[2]. Upon membrane depolarization, L-type $Ca^{2+}$ channels (LTCCs), housed within T-tubule membranes, open and release extracellular $Ca^{2+}$ into the dyadic cleft—the confined, 12 nm wide space that separates T-tubules from jSR. This localized increase in $Ca^{2+}$ activates RYR2 to release $Ca^{2+}$ from the jSR lumen into the dyadic cleft[3], from which it subsequently diffuses to stimulate the contraction of adjacent sarcomeres. Dyads are precisely positioned at the Z-disc of sarcomeres so that $Ca^{2+}$ released from dyads coordinatively activates sarcomeres throughout the cardiomyocyte in response to membrane depolarization.

Human heart disease from diverse aetiologies causes structural abnormalities of dyads, including T-tubule loss, physical uncoupling between the T-tubules and the jSR, and their displacement from Z-lines[4–9]. The resulting reduction in the magnitude of the $Ca^{2+}$

[1]Institutes of Biomedical Sciences, Department of Cardiology, Zhongshan Hospital, Fudan University, Shanghai Institute of Cardiovascular Diseases, Shanghai, China. [2]Department of Cardiology, Boston Children's Hospital, Boston, MA, USA. [3]Department of Cardiology, the First Affiliated Hospital, Sun Yat-sen University, Guangzhou, China. [4]State Key Laboratory of Biocatalysis and Enzyme Engineering, School of Life Science, Hubei University, Wuhan, China. [5]Department of Cardiology, the First Affiliated Hospital, Xi'an Jiaotong University, Xi'an, China. [6]Disease Biophysics Group, John A. Paulson School of Engineering and Applied Sciences, Harvard University, Boston, MA, USA. [7]Department of Biology, Program in Cell and Molecular Biology, Boston University, Boston, MA, USA. [8]Department of Medicine, Cardiovascular Institute, Perelman School of Medicine, University of Pennsylvania, Philadelphia, PA, USA. [9]Harvard Stem Cell Institute, Cambridge, MA, USA. ✉e-mail: fujianlu@fudan.edu.cn; william.pu@cardio.chboston.org

https://doi.org/10.1038/s41551-024-01253-z

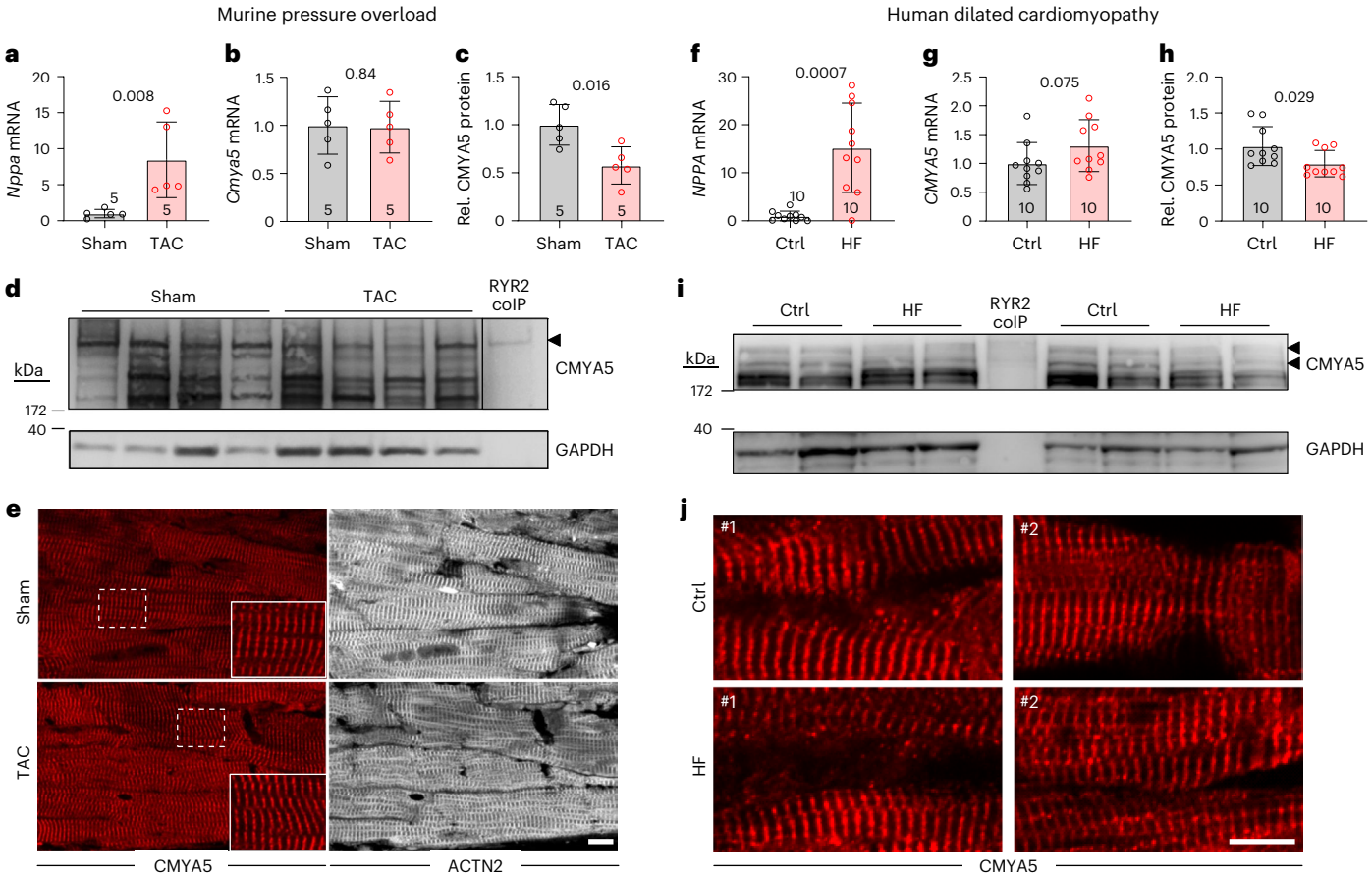


**Fig. 1 | CMYA5 expression and localization in heart failure.** Murine (**a**–**e**) and human (**f**–**j**) heart samples were analysed. **a**,**b**, Relative expression of *Nppa* (**a**) and *Cmya5* mRNA (**b**), normalized to *Gapdh*, in Sham and TAC mice. **c**,**d**, Quantification of cardiac CMYA5 protein levels. Western blots of Sham and TAC heart lysates were analysed to compare CMYA5 levels, normalized to GAPDH loading control (**c**). A representative blot is shown (**d**). The RYR2 co-IP sample, generated by immunoprecipitation of heart lysate with RYR2 antibody, identifies the CMYA5 band (arrowhead) that interacts with RYR2. **e**, CMYA5 localization in Sham and TAC myocardium. Representative images of myocardial sections immunostained with CMYA5 and Z-line component ACTN2. $n = 5$ per group. Boxed areas are magnified in insets. **f**,**g**, Relative expression of *NPPA* (**f**) and *CMYA5* (**g**) mRNA, normalized to *GAPDH*, in human HF and Ctrl left ventricular myocardium. **h**,**i**, CMYA5 protein level (**h**) in human HF and Ctrl myocardium measured by western blotting (**i**). RYR2 co-IP sample, generated by immunoprecipitating Ctrl lysate with RYR2 antibody, marks CMYA5 bands (arrowheads) that interact with RYR2. **j**, CMYA5 localization in HF and Ctrl myocardium. Images of myocardial sections immunostained with CMYA5 antibody. Two representative results from 10 samples per group are shown. Mann–Whitney test. Scale bar, 10 µm. Graphs indicate mean ± s.d. Decimals above bar graphs indicate *P*-values.

transient, depletion of SR $Ca^{2+}$ stores and desynchronized and inhomogeneous jSR $Ca^{2+}$ release lead to contractile dysfunction and arrhythmias[10,11]. Dyad architecture is also markedly deficient in cardiomyocytes derived from human induced pluripotent stem cells (hiPSC-CMs), which limits their applications for cardiac disease modelling and therapeutic heart regeneration. Methods to promote dyad assembly and stability would thus protect against cardiac remodelling and heart failure and would increase the research and therapeutic potential of hiPSC-CMs. We previously reported that the large protein CMYA5 (cardiomyopathy-associated protein 5) is required to assemble jSR adjacent to Z-lines, the first step in dyad assembly[12]. Here we show that CMYA5 levels are reduced in human and experimental heart failure. To buttress CMYA5 expression in the diseased heart, we engineered a miniaturized form of CMYA5 that can be delivered by viral vectors. We show that the expression of 'miniCMYA5' reinforces dyads in pressure-overloaded hearts and initiates dyad assembly in hiPSC-CMs.

## Results

### CMYA5 loss in heart failure

Previously, we found that *Cmya5* ablation in mice ($Cmya5^{KO}$) disrupts dyad architecture, dyad positioning at Z-lines and jSR $Ca^{2+}$ release, leading to progressive cardiac dysfunction and intolerance to pressure overload stress[12]. We investigated changes in CMYA5 that might participate in dyad disruption in diseased hearts using a mouse model in which transverse aortic constriction (TAC) induces pressure overload and cardiac dysfunction. As expected, TAC induced marked upregulation of cardiac stress marker *Nppa* compared with sham controls (Fig. 1a). *Cmya5* mRNA level was comparable between TAC and Sham (Fig. 1b). CMYA5 western blotting revealed multiple immunoreactive protein bands not present in $Cmya5^{KO}$ hearts (Supplementary Fig. 1a, Input). However, only the largest isoform co-immunoprecipitated with RYR2 (Supplementary Fig. 1a, RYR2 IP), indicating that this isoform uniquely bridges jSR to Z-lines. Quantification of this isoform demonstrated that in TAC, it was reduced to 0.57 of Sham values (Fig. 1c,d). Cardiac immunostaining demonstrated that CMYA5 localization at cardiac Z-lines, marked by ACTN2, was not altered by TAC (Fig. 1e). Localization of FSD2, a protein closely related to the C-terminal portion of CMYA5 (see below)[13], also was not altered by TAC (Supplementary Fig. 1b). However, consistent with previous studies[9], TAC disrupted RYR2 organization (Supplementary Fig. 1c). In Sham, we observed a close correlation between RYR2 and CMYA5 immunostaining signal (Supplementary Fig. 1c,d). In contrast, in TAC, this correlation was reduced and foci of RYR2 immunoreactivity without CMYA5 signal were

observed, indicative of 'orphaned' RYR2 that had lost association with CMYA5 (Supplementary Fig. 1c,d) probably due to CMYA5 insufficiency.

We then examined the expression of CMYA5 protein in human ventricles of patients with heart failure (HF) due to dilated cardiomyopathy compared with non-failing heart transplant donor controls (Ctrl; Supplementary Table 1). As seen in the murine TAC model, *NPPA* mRNA was strongly upregulated in HF compared with Ctrl, while *CMYA5* mRNA was not significantly changed (Fig. 1f,g). In human cardiac lysates, the largest two CMYA5 immunoreactive bands co-immunoprecipitated with RYR2 (Supplementary Fig. 1e). Quantification showed that these CMYA5 protein isoforms were significantly downregulated in HF compared with Ctrl (Fig. 1h,i). As in the murine TAC model, CMYA5 localization in a Z-line pattern was similar between human HF and control myocardium (Fig. 1j), whereas RYR2 localization was disrupted (Supplementary Fig. 1f).

Together, these data indicate that human dilated cardiomyopathy and murine TAC share reduced levels of CMYA5 protein capable of binding RYR2 and bridging between cardiac Z-lines and jSR. We hypothesized that bolstering CMYA5 protein could protect dyad architecture in cardiac disease.

## Engineering of a miniaturized CMYA5 derivative that retains full function

Because it efficiently transduces cardiomyocytes, adeno-associated virus (AAV) is the leading cardiac gene transfer vector, with cardiac and skeletal muscle-targeted therapies currently in clinical trials[14]. AAV's limited cargo capacity (~4.7 kb) precludes its use to express full-length CMYA5 (11.2 kb). To engineer a CMYA5 derivative that could be delivered by AAV, we analysed CMYA5 amino acid conservation across different species. Conserved residues are confined to N- and C-terminal regions (Fig. 2a). A previously studied C-terminal fragment, MD9 (residues 2,731–3,739), contains the most highly conserved regions, including a TRIM (tripartite motif family) domain and a RYR2 interaction domain[13]. In addition, N-terminal residues 78–319 are also conserved. We used AAV and the cardiomyocyte selective *Tnnt2* promoter to express NT (residues 1–329), a C-terminal fragment including MD9 (2,731–3,739), or an NT-MD9 fusion protein, which we named 'miniCMYA5', in wild-type (WT) and *Cmya5*$^{KO}$ mice. In WT cardiomyocytes, the MD9 and NT fragments each co-localized with Z-line marker ACTN2 (Supplementary Fig. 2a). In *Cmya5*$^{KO}$ cardiomyocytes, loss of CMYA5 disrupted the Z-line pattern of RYR2 localization, as we described previously[12] (Fig. 2b). NT continued to localize in a Z-line pattern, but MD9 did not. Instead, it co-localized with abnormally positioned RYR2 (Fig. 2b), probably because it binds RYR2 through its RYR2 interaction domain (Supplementary Fig. 2b). The NT fragment was sufficient to co-localize with ACTN2 at Z-lines in WT and *Cmya5*$^{KO}$ cardiomyocytes (Fig. 2b and Supplementary Fig. 2a), but it did not reverse RYR2 mislocalization (Fig. 2b), probably since it lacks the RYR2 interaction domain and did not interact with RYR2 (Supplementary Fig. 2b). In miniCMYA5, fusion of NT to MD9 yielded an engineered protein that was small enough for AAV delivery and that interacted with RYR2 (Supplementary Fig. 2b), rescued RYR2 localization in *Cmya5*$^{KO}$ cardiomyocytes (Fig. 2b) and co-localized with ACTN2 at Z-lines (Fig. 2b,c). T-tubules are also disordered in *Cmya5*$^{KO}$ (Fig. 2d). As with RYR2/jSR positioning, T-tubule organization was rescued by AAV-mediated expression of miniCYMA5, but not NT or MD9 (Fig. 2d). These results, summarized in Fig. 2e, indicate that miniCMYA5, containing the NT domain for Z-line localization, RYR2 interaction domain and TRIM domain for dimerization and interaction with other proteins[13,15,16], functionally replaces full-length CMYA5 to allow normal dyad assembly and positioning at Z-lines in *Cmya5*$^{KO}$ cardiomyocytes.

To evaluate miniCMYA5's ability to functionally replace full-length CMYA5 in the heart, we transduced *Cmya5*$^{KO}$ and WT littermates with AAV expressing miniCMYA5 or GFP (control). By echocardiography, *Cmya5*$^{KO}$ mice treated with AAV-GFP had reduced systolic heart function at 3 months compared with WT littermates, and treatment with AAV-miniCMYA5 prevented this dysfunction (Fig. 2f). *Cmya5*$^{KO}$ also developed cardiac hypertrophy, as demonstrated by increased heart-to-body-weight ratio, which was prevented by AAV-miniCMYA5 (Fig. 2g).

These data demonstrate that miniCMYA5 functionally replaces full-length CMYA5 to support normal dyad assembly, localization at Z-lines and cardiac function.

## AAV-miniCMYA5 mitigates pressure overload-induced cardiac dysfunction

To test the therapeutic potential of AAV-miniCMYA5, we administered it or AAV-luciferase (AAV-Ctrl) to P2 (postnatal day 2) mice at the dose of $1 \times 10^{11}$ viral genomes (vg) per gram body weight (Fig. 3a). At 3 months old, these mice were subjected to Sham or TAC surgery. Heart function was subsequently monitored by echocardiography, and tissue was analysed at 8 weeks post surgery. Western blotting confirmed AAV-mediated miniCMYA5 expression at 80% of the level of the endogenous RYR2-interacting CMYA5 isoform (Supplementary Fig. 2c). Endogenous CMYA5 expression was unaltered by miniCMYA5 (Supplementary Fig. 2c,d). Immunostaining demonstrated an average transduction of 61.5% of ventricular cardiomyocytes (Supplementary Fig. 2e).

In initial experiments, we tested the ability of miniCMYA5 to normalize cardiac dysfunction of *Cmya5*$^{KO}$ mice caused by TAC. Before TAC, mild cardiac dysfunction in *Cmya5*$^{KO}$ mice was normalized by miniCMYA5 (Fig. 3b, 0 w, and Extended Data Fig. 1a). At 5 and 8 weeks after TAC, AAV-Ctrl hearts had severe dysfunction (Fig. 3b and Extended Data Fig. 1a,b) and hypertrophy (Fig. 3c). Cardiac function and hypertrophy were significantly improved in AAV-miniCMYA5 hearts (Fig. 3b,c and Extended Data Fig. 1a,b). In situ imaging of T-tubule and RYR2 organization demonstrated disorganization in sham-operated *Cmya5*$^{KO}$ hearts, which deteriorated markedly after TAC (Fig. 3d). Quantitative analysis confirmed TAC-induced disorganization of T-tubules and RYR2 (reduced transverse fraction and increased longitudinal fraction; Fig. 3e) and demonstrated that these changes were significantly mitigated by miniCMYA5. Disordered dyads led to aberrant $Ca^{2+}$ release in both Sham and TAC *Cmya5*$^{KO}$ cardiomyocytes that was ameliorated by miniCMYA5, especially under isoproterenol stimulation, as indicated by miniCMYA5 reduction of $Ca^{2+}$ spark signal mass, the space–time integral of the spark signal (Fig. 3f). As a result, SR load of both Sham and TAC *Cmya5*$^{KO}$ cardiomyocytes was significantly greater with miniCMYA5 treatment (Extended Data Fig. 2a,b). In turn, the amplitude of $Ca^{2+}$ transients of both Sham and TAC *Cmya5*$^{KO}$ cardiomyocytes was significantly higher with miniCMYA5 treatment (Extended Data Fig. 2c,d), as was cardiomyocyte contractility (Extended Data Fig. 2e,f). These results indicate that CMYA5 is required to organize both jSR and T-tubular components of dyads and is essential for cardiomyocyte structural and functional integrity in the face of biomechanical stress, and that miniCMYA5 functionally substitutes for endogenous full-length CMYA5.

Since dyad disorganization is a shared feature of heart diseases of diverse aetiologies and contributes to cardiac dysfunction and arrhythmia, heart-specific delivery of miniCMYA5 may be a novel cardioprotective avenue for forms of heart disease. We investigated miniCMYA5's therapeutic potential by assessing its ability to protect WT mice from TAC-induced cardiac stress. AAV-miniCMYA5 did not significantly alter the function of unstressed mice (Fig. 3g, 0 w, and Extended Data Fig. 1c), indicating that this level of overexpression is not cardiotoxic. TAC induced moderate cardiac dysfunction in WT mice treated with AAV-Ctrl. In comparison, AAV-miniCMYA5 increased cardiac fractional shortening, a measure of systolic function, by ~1.9-fold (Fig. 3g, 8 w, and Extended Data Fig. 1c,d). Likewise, TAC induced severe hypertrophy of WT mice treated with AAV-Ctrl, which was significantly reduced by AAV-miniCMYA5 (Fig. 3h). In situ T-tubule

https://doi.org/10.1038/s41551-024-01253-z

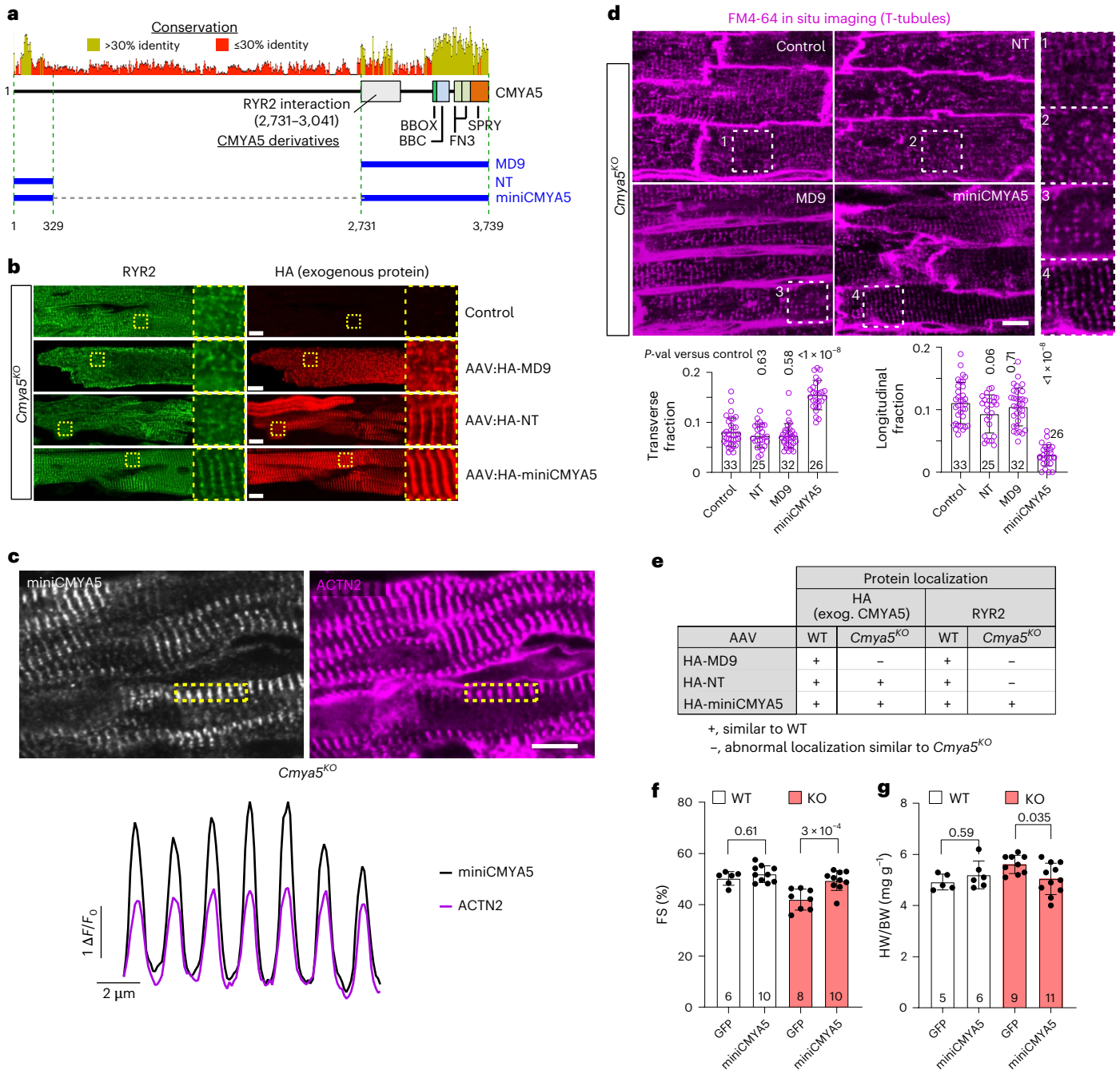


**Fig. 2 | MiniCMYA5 rescues *Cmya5*$^{KO}$ cardiomyocytes. a**, Conservation and domain structure of CMYA5. Plot shows % amino acid identity in a 20-residue sliding window between vertebrates (snake, zebrafish, frog, chicken, platypus, mouse, rat, human). Names and amino acid coordinates of truncated variants used in this study are indicated in blue. **b**, Co-localization of RYR2 and exogenous CMYA5 derivatives in *Cmya5*$^{KO}$ ventricular cardiomyocytes. RYR2 and HA staining of the same cells is shown in left and right column. Boxed areas are magnified at right. **c**, miniCMYA5 co-localization with ACTN2. Immunostaining of miniCMYA5 and ACTN2 in *Cmya5*$^{KO}$ heart sections. Spatial profile of miniCMYA5 and ACTN2 signal within the boxed area is plotted at the bottom. **d**, miniCMYA5 rescue of T-tubules organization in *Cmya5*$^{KO}$ myocardium. After plasma membrane labelling by FM4-64, 1.5-month-old hearts were optically sectioned using a confocal microscope. Bottom: transverse and longitudinal T-tubule fractions. ANOVA with Dunnett's test versus control. **e**, Summary of localization data in WT or *Cmya5*$^{KO}$ ventricular cardiomyocytes. **f**,**g**, Effect of AAV9-mediated expression of the indicated proteins on heart systolic function (fractional shortening, FS%) (**f**) and heart weight normalized to body weight (HW/BW) (**g**) at 3 months old. ANOVA with Sidak's multiple comparison test. Scale bar, 10 µm. Graphs indicate mean ± s.d. exog., exogenous.

and RYR2 imaging demonstrated TAC-induced dyad disorganization, which was significantly ameliorated by AAV-miniCMYA5 (Fig. 3i,j). Disruption of dyad architecture resulted in more aberrant spark firing at baseline and under isoproterenol stimulation (Fig. 3k), which decreased SR $Ca^{2+}$ stores (Extended Data Fig. 2g), blunted $Ca^{2+}$ transient amplitude (Extended Data Fig. 2h) and weakened cardiomyocyte contractility (Extended Data Fig. 2i). These effects were improved by AAV-miniCMYA5 (Fig. 3k and Extended Data Fig. 2g–i).

Together, these results show that bolstering CMYA5 activity in the TAC cardiac disease model by AAV-miniCMYA5 stabilizes dyad architecture, normalizes $Ca^{2+}$ release and mitigates cardiac hypertrophy and dysfunction.

https://doi.org/10.1038/s41551-024-01253-z

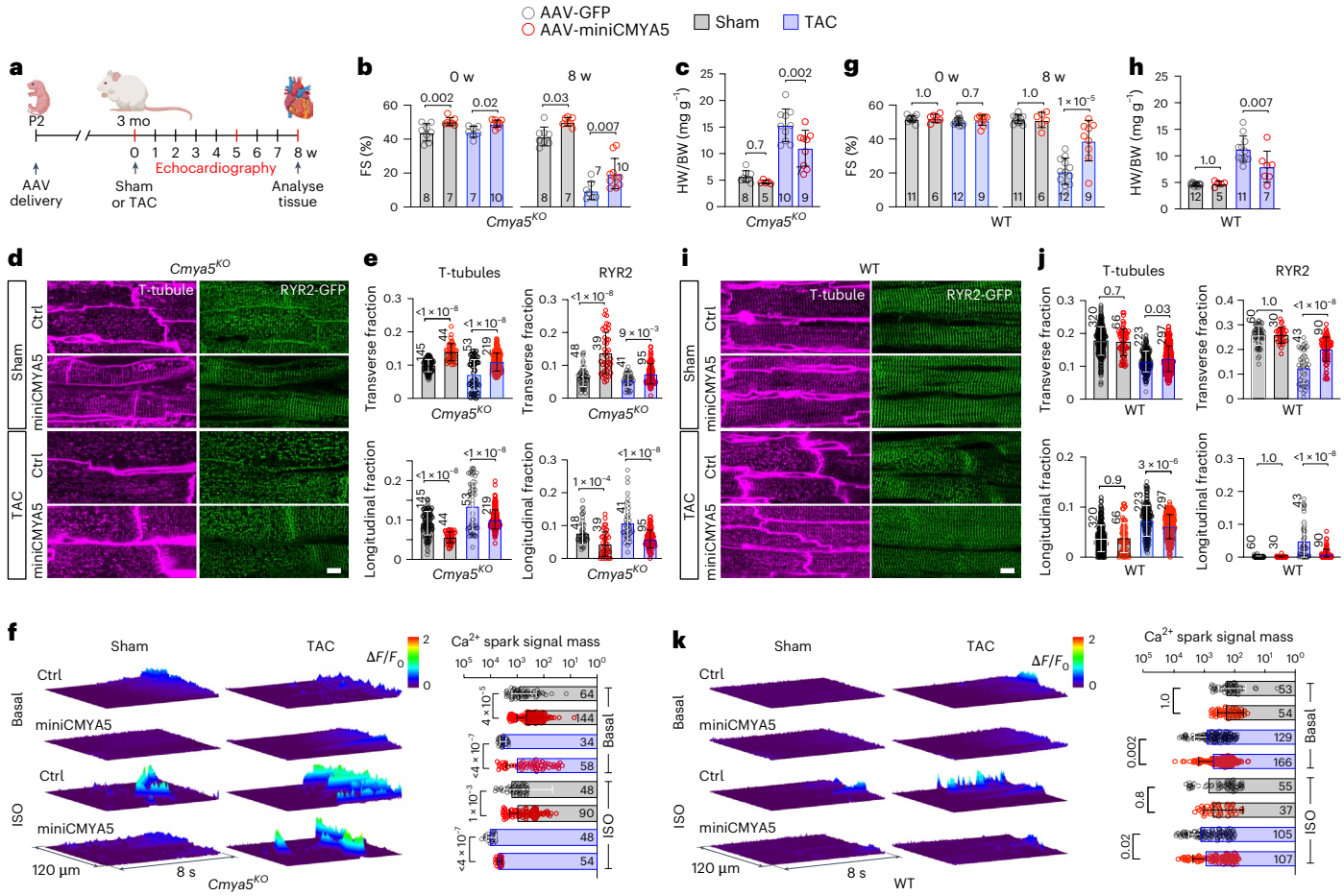


**Fig. 3 | MiniCMYA5 protects the heart from pressure overload. a**, Timeline for Sham and TAC surgery. *Cmya5*$^{KO}$ (**b**–**f**) and WT (**g**–**k**) mice were injected with AAV9-miniCMYA5 or AAV9-luciferase (Ctrl) at $1 \times 10^{11}$ vg g$^{-1}$ at postnatal day 2 (P2). At 3 months old, mice underwent baseline echocardiography (week 0) and then TAC or Sham surgery. After 8 weekly echocardiograms, necropsy was performed. Images created with BioRender.com. All mice harboured the RYR2-GFP knock-in allele. **b**,**g**, Systolic heart function of Sham and TAC mice expressing Ctrl or miniCMYA5 at 0 and 8 weeks. *Cmya5*$^{KO}$ (**b**), WT (**g**). **c**,**h**, Heart weight normalized to body weight. *Cmya5*$^{KO}$ (**c**), WT (**h**). **d**,**e**,**i**,**j**, Effect of miniCMYA5 and TAC on T-tubule and RYR2 organization. Representative in situ imaging (**d** and **i**) and quantitative analysis of the transverse and longitudinal fractions (**e** and **j**). *Cmya5*$^{KO}$ (**d** and **e**), WT (**i** and **j**). Scale bar, 10 µm. **f**,**k**, Effect of miniCMYA5 and TAC on cardiomyocyte $Ca^{2+}$ sparks. Left: representative surface plots of $Ca^{2+}$ sparks by confocal line scan imaging of Rhod2-loaded cardiomyocytes under basal conditions or with 100 nM isoproterenol (ISO). Right: $Ca^{2+}$ spark activity was quantified as the signal mass, the space–time integral of the spark signal. *Cmya5*$^{KO}$ (**f**), WT (**k**). ANOVA with Sidak's multiple comparison test (**b**, **c**, **e**, **g**, **h** and **j**). Mann–Whitney with Bonferroni multiple testing correction (**f** and **k**). Graphs indicate mean ± s.d. mo, month; w, week.

## AAV-miniCMYA5 treatment of established heart disease improves myocardial outcome

Typically, heart failure treatment is initiated to patients with established heart disease. We modelled this scenario by administering AAV-miniCMYA5 to mice 2 weeks after TAC, when mice have already developed cardiac dysfunction (Fig. 4a). TAC or Sham surgery was performed on 3-month-old WT mice. Echocardiography at 2 weeks post TAC was performed to assess cardiac dysfunction. Mice were then randomly assigned to either AAV-miniCMYA5 or AAV-luciferase (AAV-Ctrl) therapy. AAV viruses were delivered at $1 \times 10^{11}$ vg g$^{-1}$ by retro-orbital injection, which resulted in ~60% transduction efficiency (Fig. 4b). At the study endpoint of 8 weeks post TAC, echocardiography was performed followed by tissue and molecular studies. Compared with Ctrl, miniCMYA5 did not affect the cardiac function of sham-operated mice (Fig. 4c). Treatment with miniCMYA5 tended to blunt cardiac hypertrophy induced by TAC and tended to reduce pulmonary congestion, as reflected by normalized lung weights (Fig. 4d). Consistent with these physiological measurements, miniCMYA5 protected T-tubule and RYR2 organization from TAC-induced disorganization (Fig. 4e). In single dissociated cardiomyocytes, miniCMYA5 improved the SR load, $Ca^{2+}$ transient amplitude and cardiomyocyte contractility (Fig. 4f–h). These results show that miniCMYA5 gene therapy intervention improved myocardial outcome in the TAC heart disease model even when initiated after the onset of cardiac dysfunction.

## MiniCMYA5 promotes RYR2 positioning in hiPSC-CMs

hiPSC-CMs are immature and lack well-organized dyads, which limits their use in disease modelling and tissue repair. Although hormones[17–19], culture conditions[20] and bioengineering approaches[21–25] have been taken to improve hiPSC-CM maturity, so far these efforts have had limited success at improving dyad assembly. We showed that CMYA5 anchoring of RYR2/jSR to the Z-lines is an early and essential step in the development of dyads that precedes the formation of T-tubules[12]. *Cmya5* is strongly upregulated in mature compared with fetal murine cardiomyocytes (Extended Data Fig. 3a–c). Given the overall immaturity of hiPSC-CMs, we hypothesized that their low expression of CMYA5 contributes to poor dyad assembly. We found that CMYA5 transcripts are barely detectable in hiPSC-CMs (Fig. 5a), and CMYA5 protein was not detected by western blotting (Fig. 5b).

https://doi.org/10.1038/s41551-024-01253-z

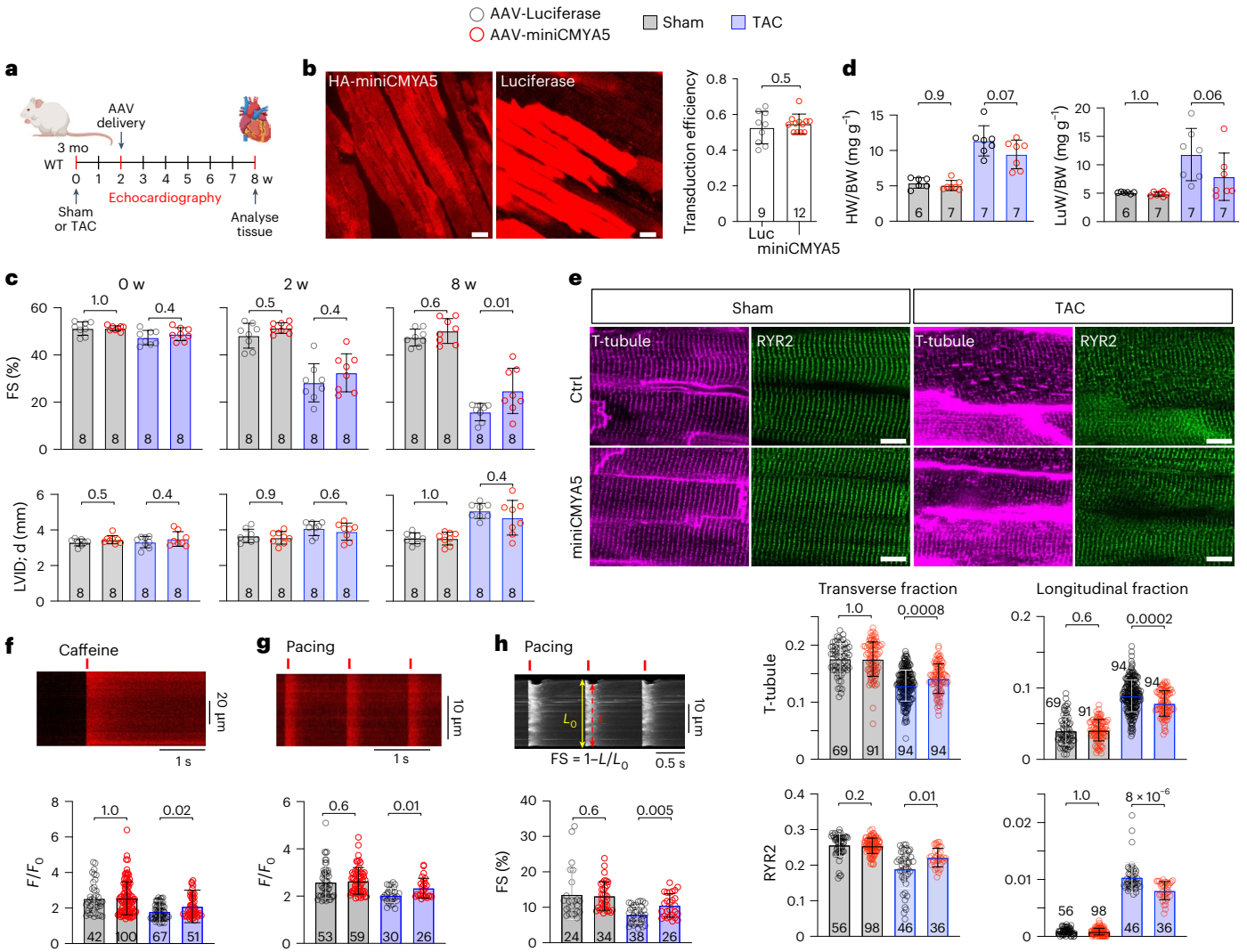


**Fig. 4 | AAV-miniCMYA5 treatment of established heart disease.** **a**, Experimental outline. Two weeks after TAC or Sham surgery, WT adult mice were randomized to receive AAV-miniCMYA5 or AAV-luciferase (control). Mice were then evaluated at 8 weeks after TAC. Images created with BioRender.com. All mice harboured the RYR2-GFP knock-in allele. **b**, Representative myocardial images (left and middle) and quantification of AAV transduction efficiency (right). Each point represents one section. At least three different sections were quantified per heart and at least three separate hearts were analysed. Scale bar, 20 µm. **c**, Echocardiography measurement of heart function. LVID;d, left ventricular internal diameter at end-diastole. **d**, Organ weights normalized to body weight. LuW, lung weight. **e**, Representative in situ confocal images (top) and quantification (bottom) of T-tubule and RYR2 organization. Scale bar, 10 µm. **f**–**h**, Individual dissociated cardiomyocytes were loaded with Rhod2, paced and analysed by confocal line scan imaging. Caffeine treatment to measure SR $Ca^{2+}$ load (**f**). $Ca^{2+}$ transients (**g**) and cardiomyocyte shortening (**h**) under 1 Hz pacing. Each point represents one cardiomyocyte. *t*-test (**b**), ANOVA with Sidak correction for two comparisons (**c** and **d**), Mann–Whitney with Bonferroni correction for two comparisons (**e**–**h**). Graphs indicate mean ± s.d. mo, month; w, week.

Organized sarcomeres are critical for cardiomyocyte maturation, and sarcomere Z-lines are the scaffold that organizes the assembly of dyads. hiPSC-CM sarcomere organization is enhanced by culturing them on extracellular matrix (ECM) rectangular islands with 7:1 aspect ratio[26–28], the geometry of de facto human ventricular cardiomyocytes[29]. Therefore, we used ECM microcontact printing to generate shape-controlled hiPSC-CMs with highly organized sarcomeres (Fig. 5c,d). We did not observe localization of RYR2 in a Z-line pattern in cells treated with negative control adenovirus (Ad:LacZ; Fig. 5e), consistent with low CMYA5 expression in hiPSC-CMs and the essential role of CMYA5 to position RYR2/jSR adjacent to Z-lines. This situation is reminiscent of fetal cardiomyocytes, which have well-organized Z-lines but incomplete alignment of RYR2 (ref. 12) in the context of low CMYA5 expression. In contrast, shape-controlled hiPSC-CMs treated with Ad:miniCMYA5 demonstrated regular alignment of miniCMYA5 with Z-lines (Extended Data Fig. 3d) and regions with RYR2 partial co-localization with miniCMYA5 in a Z-line pattern (Fig. 5e,f). Despite advancing RYR2 organization and alignment with Z-lines, we did not observe the later step of T-tubule formation (Extended Data Fig. 3e).

We evaluated the impact of improved RYR2 organization on hiPSC-CM $Ca^{2+}$ handling and force generation. We observed that miniCMYA5 treatment of patterned hiPSC-CMs increased $Ca^{2+}$ transient amplitude and shortened the time to the $Ca^{2+}$ transient peak (Fig. 5g–i). To assess whether these ultrastructural changes translated to altered force generation, the hiPSC-CMs were placed in three-dimensional (3D) culture in a fibrin gel moulded between silicone pillars[22] (Extended Data Fig. 4a). The active force generated by these engineered heart tissues (EHTs) was greater with miniCMYA5 treatment, compared with control treatment (Extended Data Fig. 4b–d).

These data demonstrate that miniCMYA5 expression in hiPSC-CMs promotes alignment of RYR2/jSR to Z-lines, an initial and essential step for dyad assembly and maintenance, which enhances hiPSC-CM $Ca^{2+}$ handling and contraction.

https://doi.org/10.1038/s41551-024-01253-z

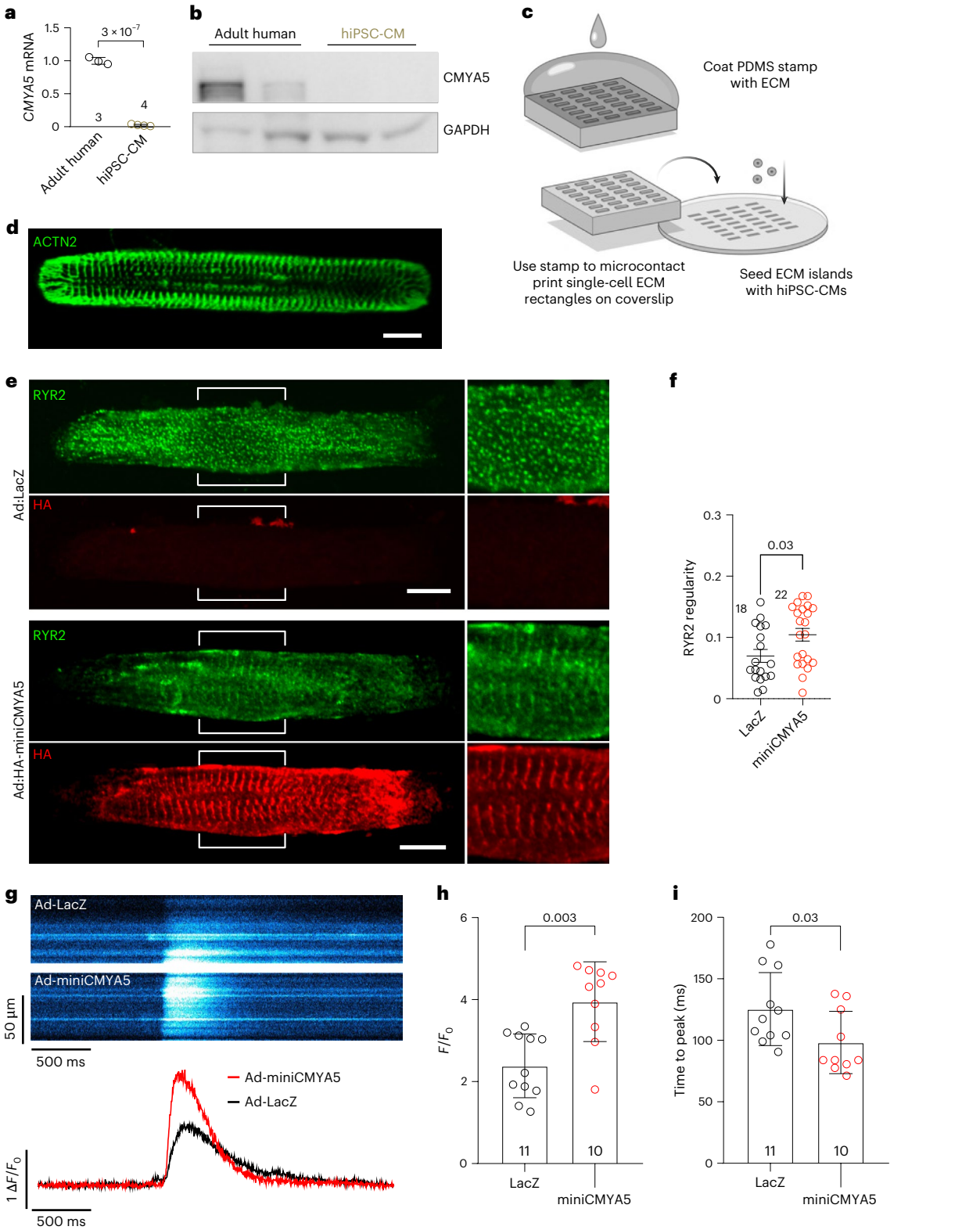


**Fig. 5 | MiniCMYA5 promotes dyad assembly in hiPSC-CMs. a**,**b**, mRNA (**a**) and protein (**b**) level of CMYA5 in adult human hearts and hiPSC-CMs. **c**, Schematic of the workflow used to generate shape-controlled hiPSC-CMs, which have highly organized Z-lines. A PDMS stamp with rectangular features is used to print extracellular matrix rectangular islands on glass coverslips. Selective adhesion patterns the hiPSC-CMs. **d**, Representative image of patterned hiPSC-CMs immunostained for Z-line marker ACTN2. **e**, Representative image of patterned hiPSC-CMs transduced with Ad:LacZ (top) or Ad:HA-miniCMYA5 (bottom) and co-immunostained for RYR2 and HA. Bracketed regions are magnified at right. Scale bar, 10 µm. **f**, Quantification of RYR2 regularity. **g**–**i**, $Ca^{2+}$ transient recordings of patterned hiPSC-CMs treated with Ad:LacZ or Ad:HA-miniCMYA5, and Ad:GCaMP6f-Junctin and paced at 1 Hz. **g**, Representative confocal line scan images (top) and $Ca^{2+}$ transient (bottom). **h**,**i**, Quantification of $Ca^{2+}$ transient amplitude (**h**) and time to peak (**i**). Each point represents a different hiPSC-CM. *t*-test (**a** and **f**), Mann–Whitney test (**h** and **i**). Graphs indicate mean ± s.d. Values above bar graphs indicate *P*-values.

## Discussion

Efficient cardiomyocyte contraction requires coupling membrane depolarization to coordinate $Ca^{2+}$ release throughout the cell. This coordination is achieved through the tight linkage between LTCCs in the T-tubules, RYR2 in the jSR and sarcomere Z-lines[2,30]. CMYA5 is required to tether RYR2 and the jSR near Z-lines[12]. Here we show that CMYA5 bridges Z-lines to RYR2/jSR through its evolutionarily conserved structure, in which the N-terminal domain recognizes Z-lines and the C-terminal region binds RYR2/jSR (Fig. 4g). The large, disordered and poorly conserved region between its conserved termini was dispensable in our assays, as fusion of the conserved N- and C-terminal regions in miniCMYA5 fully complemented *Cmya5*$^{KO}$ cardiomyocytes.

Loss of dyad architecture and subcellular localization is a common hallmark of heart disease that contributes to cardiac dysfunction and arrhythmia. Factors that destabilize T-tubules in diseased hearts, such as reduced BIN1 (ref. 31) or JPH2 expression[4], or JPH2 cleavage[32], have been implicated in the loss of T-tubule organization in diseased hearts. However, RYR2/jSR organization is also disrupted in heart failure. T-tubules are not required for RYR2/jSR organization or localization to Z-lines, and mechanisms that perturb them in heart failure were not described previously. We previously established that CMYA5 localizes to Z-lines and tethers RYR2/jSR adjacent to these structures[12]. T-tubules subsequently form and co-localize with jSR, yielding organized, properly positioned dyads. CMYA5 depletion disrupted the patterning of both RYR2/jSR and the T-tubule network[12]. Here we show that the subset of CMYA5 that interacts with RYR2 is downregulated in failing hearts, which was associated with loss of RYR2/jSR and T-tubule architecture, defective $Ca^{2+}$ signalling and impaired cardiac contraction in the pressure-overloaded heart. Reduced CMYA5 contributes to these phenotypes, since AAV-mediated expression of miniCMYA5 ameliorated pressure overload-induced dyad disorganization, aberrant $Ca^{2+}$ signalling and cardiac dysfunction.

Our results show that bolstering CMYA5 activity through AAV-mediated expression of miniCMYA5 may benefit heart disease caused by pressure overload and other pathological stresses. This result provides mechanistic insights into the pathogenesis of dyad disarray and heart disease. Furthermore, it suggests that augmenting CMYA5 activity may be a useful therapeutic strategy for cardiac dysfunction. At a transduction efficiency of 50–60%, miniCMYA5 only partially prevented or reversed TAC-induced cardiac dysfunction. The salutary effects of AAV-miniCMYA5 could be augmented using alternative promoters and capsids to transduce a higher fraction of cardiomyocytes or achieve physiological or supraphysiological levels. Additional protein engineering could further enhance its biological activity. Previous studies overexpressed JPH2 (ref. 33) and BIN1 (ref. 34) to protect dyads from pressure overload. While beneficial, these manipulations focused on T-tubule stabilization appear less potent than miniCMYA5 (Supplementary Table 2), potentially since jSR organization is upstream of T-tubules. Indeed, miniCMYA5 also improved T-tubule organization following TAC. Nevertheless, the reduction of T-tubule stabilizing factors such as JPH2 and BIN1 may also be important contributors to dyad disarray in heart disease, and combined overexpression of miniCMYA5 and JPH2 could be more effective than either therapy alone.

hiPSC-CMs fail to form dyads, which limits their use in disease modelling and tissue repair. Previously, adjustment culture media, 3D culture, and phasic, direction cell stress have been used to increase hiPSC-CM maturation, including alignment of RYR2 and formation of T-tubules[19,21–24,35]. Here we define a new facet of hiPSC-CM immaturity that contributes to impaired dyad assembly—low expression of CMYA5. Even in shape-controlled hiPSC-CMs with well-organized sarcomeres, RYR2 did not properly localize near sarcomere Z-lines. Virally expressed miniCMYA5 localized to Z-lines, enhanced hiPSC-CM RYR2/jSR Z-line co-localization, increased $Ca^{2+}$ transient amplitude and $Ca^{2+}$ upstroke velocity, and increased the contractile force of EHTs. However, RYR2 organization and dyads were only partially restored, possibly due to low expression or immaturity of other key dyad assembly proteins. Nevertheless, miniCMYA5 provides the first genetic approach to promote the structural maturation of human cardiac muscle. Future investigations are warranted to identify other factors required for dyad assembly to determine whether their co-expression can further promote dyad assembly in hiPSC-CMs. This study focused on the maturation of cardiac dyad structure and function; additional studies are required to assess whether genetic enhancement of dyad assembly more broadly enhances hiPSC-CM maturation.

## Methods

### Animals

All animal experiments were performed under protocols approved by the Boston Children's Hospital Institutional Animal Care and Use Committee. *Cmya5*$^{KO}$ (C57BL/6NJ-*Cmya5*$^{em1(IMPC)J}$/Mmja, 032826) mice were obtained from the Jackson Laboratory. *Ryr2-gfp* knock-in mice were described previously[36]. Mice were housed in a specific pathogen-free facility with 12 h/12 h light/dark cycle, 22 ± 2 °C temperature and 45%–65% relative humidity. Mice were genotyped using PCR primers shown in Supplementary Table 3.

### Echocardiography

Echocardiography was performed on a VisualSonics Vevo 3100 instrument with Vevostrain software. Animals were awake during the procedure and held in a standard handgrip. The echocardiographer was blinded to group assignment.

### Human heart procurement and tissue samples

Procurement of human myocardial tissue was performed under protocols and ethical regulations approved by Institutional Review Boards at the University of Pennsylvania and the Gift of Life Donor Program (Pennsylvania, USA) as previously described[37]. Failing hearts were obtained at the time of cardiac transplantation and all transplant patients provided prospective informed consent for use of their explanted heart tissue for research. Non-failing hearts were obtained at the time of organ donation from cadaveric donors with consent for research use of heart tissue provided by the next of kin. In vivo function, based on left ventricle ejection fraction, was assessed via echocardiography in all hearts. At the time of tissue procurement, all hearts were arrested in situ using ice-cold, blood-containing, high-potassium cardioplegic solution. Explanted hearts were transported to the laboratory on wet ice in cold Krebs–Henseleit buffer solution. Tissues were snap frozen in liquid nitrogen and stored at −80 °C until analysis.

### TAC

Aortic banding was performed on male mice between 25 and 30 g in weight using a previously described protocol[38]. Mice were anaesthetized with isoflurane, intubated and mechanically ventilated. The chest cavity was entered through an incision in the left second intercostal space. The transverse aorta was dissected from the surrounding tissues. A silk suture was passed underneath the aorta and ligated against a 27-gauge needle between the brachiocephalic trunk and the left common carotid artery. The needle was then removed, resulting in a ligature with a fixed diameter constricting the aorta. The chest cavity, muscles and skin were closed layer by layer. The sham operation was identical except that the aorta was not manipulated. The surgeon was blinded to genotype and treatment.

### AAV production and injection

Amino acid positions refer to Uniprot Q70KF4 (murine CMYA5). The NT domain corresponds to amino acids 1–329 and the MD9 domain to amino acids 2,731–3,739. In miniCMYA5, these are joined together with a bacterial linker sequence (110 aa) that was fused to the source *Cmya5* cDNA (accession AJ575748)[39]. In experiments on individual fragments, this sequence was included with the NT fragment.

The miniCMYA5 construct also had a 3x haemagglutinin (HA) epitope tag on the N terminus.

For overexpression experiments in mice, genes of interest were subcloned into AAV9-cardiac troponin T promoter vector (Addgene, 69915)[40]. For AAV production[41], the AAV plasmids along with the helper plasmids AAV9-Rep/Cap (Addgene, 112865) and pAd-ΔF6 (Addgene, 112867) were co-transfected into HEK293T cells using polyethylenimine (Polysciences, 23966-2). AAV was purified by iodixanol density gradient centrifugation. The density gradient was made by layering the following solutions in Optiseal tubes (BECKMAN COULTER, 362183): 6 ml of 17% iodixanol, 5 ml of 25% iodixanol, 4 ml of 40% iodixanol, 5 ml of 60% iodixanol. HEK293T cell lysate containing AAV was layered on top of the density gradient and centrifuged at 45,000 × *g* for 2 h. AAV was recovered from the density gradient and titred by qPCR. AAV was then injected into P2 (postnatal day 2) pups subcutaneously in a total volume of less than 30 µl at a full dose of $1 \times 10^{11}$ vg $g^{-1}$. For adult mice, AAV was delivered by retro-orbital injection at a dose of $1 \times 10^{11}$ vg $g^{-1}$.

### Recombinant adenovirus production and infection

MiniCMYA5 carrying 3x HA tag was amplified from the AAV vector and inserted into pENTR/TEV/D-TOPO vector (Invitrogen, K252520). Adenovirus was produced using the Invitrogen adenoviral expression system (Invitrogen, V49320) and purified using the Vivapure AdenoPack (Sartorius, VS-AVPQ020). Cultured cells were treated with adenovirus at a multiplicity of infection (MOI) of 20.

### RNA extraction and quantitation

Total RNA was isolated using Direct-zol RNA Miniprep Plus kits (Zymo Research, R2071). DNase I-pretreated RNA (1 µg) was used as input for reverse transcription using SuperScript III First-strand Synthesis SuperMix (Thermo Fisher, 18080400). Gene expression was analysed by qPCR using Power SYBR Green PCR Master Mix (Applied Biosystems, 4367659) and a Bio-Rad CFX96 touch thermocycler, using qPCR primers listed in Supplementary Table 3.

### Western blotting

Cell lysates (50 µg) were separated by 4–12% SDS–PAGE (Invitrogen, NW04120BOX) and transferred to Immobilon-P PVDF membranes (Merck Millipore, IPVH00010). The membranes were blocked with 5% non-fat dry milk and incubated with primary antibody (Supplementary Table 4) overnight at 4 °C, followed by incubation with secondary antibody for 1 h at room temperature. Western blot signals were captured using a Fujifilm LAS-3000 imager and quantified using Fiji.

### Co-immunoprecipitation assays

For 500 µg tissue lysates, 50 µl protein G beads (Invitrogen, 10003D) and 5 µl primary antibody (1 mg $ml^{-1}$) IgG control were used. Beads were washed for 10 min in 600 µl PBS, then incubated with protein and antibodies overnight at 4 °C. The protein-bound beads were washed with immunoprecipitation buffer (Thermo Fisher, 87787) containing protease inhibitor (Thermo Fisher, A32965) extensively for 10 times and subsequently boiled at 100 °C for 10 min to release targets.

### In situ confocal imaging of cardiomyocyte T-tubule and RYR2 localization in intact hearts

For in situ T-tubule imaging[42], intact mouse hearts underwent Langendorff perfusion at room temperature with 0 $Ca^{2+}$ Tyrode solution (in mM, pH 7.4: NaCl 137, glucose 15, HEPES 20, KCl 4.9, $MgCl_2$ 1.2, $NaH_2PO_4$ 1.2) containing 10 mM 2,3-butanedione monoxime (BDM) and 2.5 µM FM4-64 (Invitrogen, T3166), a lipophilic fluorescent indicator of the plasma membrane, for 20 min. The hearts were then placed in a perfusion chamber mounted on the stage of an Olympus FV3000RS confocal microscope and imaged in situ with a ×60 (NA = 1.4) oil immersion lens. The optical pinhole was set to 1 airy disc (<1 µm axial resolution). Excitation for FM4-64 and RYR2-GFP was 488 nm, and emission was 680–780 nm and 490–540 nm, respectively.

### Mouse cardiomyocyte isolation

Single ventricular myocytes were enzymatically isolated from mouse hearts. Hearts were excised from isoflurane-anaesthetized animals, rinsed in cold perfusion buffer (PB, in mM, pH 7.4: NaCl 137, glucose 15, HEPES 20, KCl 4.9, $MgCl_2$ 1.2, $NaH_2PO_4$ 1.2, taurine 5 and BDM 10) and quickly mounted on a Langendorff perfusion system. Hearts were then perfused at 37 °C with oxygenated $Ca^{2+}$-free PB (gassed with 95% $O_2$, 5% $CO_2$) until blood was completely cleared (~5 min). The solution was then switched to digestion solution (PB containing 0.7 mg $ml^{-1}$ type II collagenase (Worthington, LS004176), 0.1 mg $ml^{-1}$ type XIV protease (Sigma-Aldrich, P5147), 1 mg $ml^{-1}$ bovine serum albumin (BSA, Sigma-Aldrich, A3912) and 50 µM $Ca^{2+}$). Once hearts became soft (~15–30 min), perfusion was stopped and ventricles were gently minced into small pieces and agitated by blunt-tipped transfer pipettes in PB containing 1 mg $ml^{-1}$ BSA and 50 µM $Ca^{2+}$. Cells were filtered using a 100 µm cell strainer (Fisher Scientific, 0877119), centrifuged for 1 min at 20 *g* and subjected to $Ca^{2+}$ gradient recovery using PB containing 1 mg $ml^{-1}$ BSA and $Ca^{2+}$ from 0.25, 0.35, 0.52 to 1 mM sequentially.

Coverslips were pre-coated with 5 µg $ml^{-1}$ laminin (Sigma-Aldrich, L2020) for at least 30 min at 37 °C. Freshly isolated myocytes were plated onto the coverslips for 30 min in the incubator. Attached mouse cardiomyocytes were cultured in MEM medium (Sigma-Aldrich, M2279) supplemented with 10 mM BDM.

### $Ca^{2+}$ dye loading and live cell imaging

To record cytosolic $Ca^{2+}$ signals, freshly isolated murine cardiomyocytes were incubated with $Ca^{2+}$ indicator Rhod2-AM (5 µM, Invitrogen, R1244) at 37 °C for 10 min (ref. 43) and then gently washed twice. Dye loading, washing and $Ca^{2+}$ imaging were conducted in Tyrode solution containing 1 mM $Ca^{2+}$. For $Ca^{2+}$ transient and SR load measurement, 10 mM BDM was added to avoid motion artefact. Caffeine (10 mM) was introduced to deplete the SR store. For spark recording and contractility assay, BDM was not provided. Isoproterenol (100 nM) was applied when needed in spark recording. For $Ca^{2+}$ transient recording in patterned hiPSC-CMs, cells were infected with adenovirus carrying GCaMP6f-Junctin[43] (MOI = 10) and paced at 1 Hz.

Confocal imaging was performed with an Olympus FV3000RS microscope with a ×60 (NA = 1.4) oil immersion objective and a line scan speed of 4 ms per line for a total 8 s duration. The pinhole was set for a nominal 1 µm optical section. For measurement of Rhod2 signal, excitation was at 543 nm and fluorescence emissions were collected at >560 nm. GCaMP6f-Junctin was excited at 488 nm and emissions were collected at 520–560 nm.

### Differentiation of hiPSC-CMs

WTC-11 normal human male iPSCs (Coriell Institute, GM25256) that harbour a doxycycline (Dox)-inducible CRISPR/Cas9 have been described previously[44]. These cells were maintained in Essential 8 medium (Thermo Fisher, A1517001). hiPSC-CMs were differentiated as described previously[45]. Briefly, cells were washed once with PBS, detached by incubation with Versene (Invitrogen, 15040066) for 5–10 min and seeded onto 12-well plates pretreated with 1:100 (v/v) diluted Geltrex (Life Technologies, A1413302) at a density of 10,000 cells per $cm^2$ in E8 medium supplemented with 10 µM of ROCK inhibitor Y-27632 (R&D, 1254). When cell confluency reached ~50–60%, cells were treated with basic medium RPMI 1640 (Life Technologies, 61870127) plus 1x B27 minus insulin (Life Technologies, A1895601) containing 7 µM CHIR99021 (STEMCELL Technologies, 72054) for 48 h, followed by basic medium containing 5 µM IWR-1-endo (STEMCELL Technologies, 72564) for another 48 h. On day 7 of differentiation, cells were cultured in basic medium supplemented with 1:1,000 (v/v) insulin

(Sigma-Aldrich, I9278). Finally, cells were dissociated for 1–2 h depending on cell density using collagenase II (Worthington, LS004176).

### hiPSC-CM patterning

Micropatterns were produced on glass coverslips (12 mm, VWR, 48366-252) coated with a 1:1 ratio of polydimethylsiloxane (PDMS) 184 (10:1 elastomer base:curing agent, The Dow Chemical Company LT, H047M73001) and 527 (1:1 Part A:Part B, The Dow Company LT, H047L6A013). Coverslips were coated for 48 h in a 65 °C oven and then exposed to UV ozone for 8 min. Then, stamps with rectangular features (7:1 aspect ratio, 1,600 $\mu m^2$ area) were coated for 1 h with fibronectin (50 $\mu g\ ml^{-1}$) diluted in Geltrex (1:200, Life Technologies, A1413302). The dried stamps were then placed on PDMS-coated coverslips. Pluronics F-127 (1%; Sigma-Aldrich, P2443) was used to wash the coverslips for 10 min, followed by washing 3 times with room-temperature PBS.

Cells ($1 \times 10^6$) were seeded into a well of a 12-well plate. Virus was incubated with seeded cells for 48 h at MOI 20. Cells were then dissociated into single cells using the cardiomyocyte dissociation kit (STEMCELL Technologies, 05025), and 50,000 cells were seeded onto each glass coverslip. Cells were cultured for 5 days and then fixed for immunofluorescence assays.

### Engineered human heart tissue fabrication, culture and contractile force assessment

To generate 3D human cardiac tissue bundles, we adapted a previously described protocol[22]. PDMS ($14 \times 12\ mm^2$; Dow Corning, SYLGARD184) moulds with Velcro frame (1.2 mm long) were used. hiPSC-CMs were dissociated to single cells using 0.2% collagenase type I (Sigma, 0130) and 0.25% trypsin/EDTA (Gibco, 25200056). Hydrogel solution containing 24 µl 10 $mg\ ml^{-1}$ fibrinogen (Sigma, F3879), 12 µl Matrigel (Corning, 354277) and 24 µl 2x cardiac medium were mixed with $1 \times 10^6$ hiPSC-CMs and adenovirus (MOI = 10) in 58 µl 1x cardiac medium and 2.4 µl 50 U $ml^{-1}$ thrombin (Sigma, T7201) to obtain a total of ~120 µl cell/gel mixture. A 1x cardiac medium is composed of 2 $\mu g\ ml^{-1}$ vitamin B12 (Sigma, V6629), 1 $mg\ ml^{-1}$ 6-aminocaproic acid (Sigma, A2504), 10% fetal bovine serum (FBS, ABW, LT22906) and low-glucose DMEM (Gibco, 1567014). The mixture was placed in the moulds at 37 °C for 1 h to polymerize. RPMI 1640 medium (Gibco, 11875093) with 1 mM sodium pyruvate (Gibco, 11360070), 0.45 µM 1-thioglycerol (Sigma, M6145), 0.1 mM non-essential amino acids (Gibco, 11140050), 2 $mg\ ml^{-1}$ 6-aminocaproic acid, 0.4 $mg\ ml^{-1}$ ascorbic acid (Sigma, A4544) and 1% penicillin-streptomycin (Gibco, 15140122) supplemented with 5% FBS was used to culture the tissues. The force-generating capacity of the engineered heart tissues was assessed on day 10 by loading into a customized mechanical test system. Inotropic responsiveness of the tissue bundles was tested by measuring contractile force generation in 1.8 mM $Ca^{2+}$ Tyrode solution during electrical stimulation at 2 Hz. The bundles were stretched using a linear actuator from 0% to 8% above the resting length in 2% increments.

### Immunofluorescence assays

Hearts were fixed in 4% paraformaldehyde (PFA) overnight and allowed to sink in 30% sucrose (typically 3–4 h) before freezing in tissue freezing medium (TFM, General Data). Cryo-sections (10 µm thick) were affixed to slides. Heart sections were permeabilized with 0.5% Triton X-100 for 20 min and blocked with 10% normal goat serum for 1 h. Seeded isolated cells were fixed in 2% PFA for 15 min at room temperature, washed 3 times with PBS, permeabilized with 0.1% Triton X-100 for 10 min, then rinsed 3 times with PBS and blocked with 1% BSA for 1 h. The sections or cells were then incubated with primary antibody (Supplementary Table 4) overnight at 4 °C, washed with PBS 3 times, incubated with Alexa fluor dyes-conjugated donkey secondary antibody (Invitrogen, 1:200) for 2 h at room temperature, washed with PBS 3 times and then incubated with 1 $mg\ ml^{-1}$ 4′,6-diamidino-2-phenylindole (DAPI) for 10 min at room temperature. Immunofluorescence staining was visualized using a confocal microscope at 405 nm (DAPI), 488 nm (Alexa fluor 488), 543 nm (Alexa fluor 555) and 647 nm (Alexa fluor 647) excitation, and 420–470 nm, 490–520 nm, 560–620 nm and >650 nm emission, respectively.

### RNA-seq

Gene expression values during normal development were obtained by RNA-sequencing of purified ventricular cardiomyocytes. The data were reported previously[46] and are available from GEO, accession number GSE195902.

### Image processing and analysis

T-tubule, RYR2-GFP and $Ca^{2+}$ imaging[47] data were analysed using custom code written in Interactive Data Language (ITT). RYR2 regularity of shape-controlled iPSC-CMs was measured using the sarcomere packing density algorithm, as described previously[27]. EHT contraction data were analysed using Matlab. The custom code is provided as Supplementary Code.

### Statistics and reproducibility

Each experiment was repeated independently with similar results at least 2 times, or as specified in the figure legends. Measurements were made with investigators blinded to group assignment. Two-sided Student's *t*-test and analysis of variance (ANOVA) were used for normally distributed data, and two-sided Mann–Whitney or Kruskal–Wallis non-parametric tests were used otherwise. $P < 0.05$ was considered statistically significant. Statistical analysis was performed using GraphPad Prism 10. Results are displayed as mean ± s.d. Sample sizes indicate independent biological replicates. Graphs show mean ± s.d.

### Reporting summary

Further information on research design is available in the Nature Portfolio Reporting Summary linked to this article.

## Data availability

The data supporting the results in this study are available within the paper and its Supplementary Information. The raw and analysed datasets generated during the study are available for research purposes from the corresponding authors on reasonable request. Source data are provided with this paper.

## Code availability

Custom code is provided as Supplementary Information and is also available in Zenodo at https://doi.org/10.5281/zenodo.13366870 (ref. 48).

## References

1. Hong, T. & Shaw, R. M. Cardiac T-tubule microanatomy and function. *Physiol. Rev.* **97**, 227–252 (2017).
2. Lu, F. & Pu, W. T. The architecture and function of cardiac dyads. *Biophys. Rev.* **12**, 1007–1017 (2020).
3. Cheng, H. & Lederer, W. J. Calcium sparks. *Physiol. Rev.* **88**, 1491–1545 (2008).
4. Zhang, H.-B. et al. Ultrastructural uncoupling between T-tubules and sarcoplasmic reticulum in human heart failure. *Cardiovasc. Res.* **98**, 269–276 (2013).
5. Wei, S. et al. T-tubule remodeling during transition from hypertrophy to heart failure. *Circ. Res.* **107**, 520–531 (2010).
6. Crossman, D. J., Ruygrok, P. N., Soeller, C. & Cannell, M. B. Changes in the organization of excitation–contraction coupling structures in failing human heart. *PLoS ONE* **6**, e17901 (2011).
7. Louch, W. E., Sejersted, O. M. & Swift, F. There goes the neighborhood: pathological alterations in T-tubule morphology and consequences for cardiomyocyte $Ca^{2+}$ handling. *J. Biomed. Biotechnol.* **2010**, 503906 (2010).

8. Jones, P. P., MacQuaide, N. & Louch, W. E. Dyadic plasticity in cardiomyocytes. *Front. Physiol.* **9**, 1773 (2018).
9. Hadipour-Lakmehsari, S. et al. Nanoscale reorganization of sarcoplasmic reticulum in pressure-overload cardiac hypertrophy visualized by dSTORM. *Sci. Rep.* **9**, 7867 (2019).
10. Piacentino, V. et al. Cellular basis of abnormal calcium transients of failing human ventricular myocytes. *Circ. Res.* **92**, 651–658 (2003).
11. Song, L.-S. et al. Orphaned ryanodine receptors in the failing heart. *Proc. Natl Acad. Sci. USA* **103**, 4305–4310 (2006).
12. Lu, F. et al. CMYA5 establishes cardiac dyad architecture and positioning. *Nat. Commun.* **13**, 2185 (2022).
13. Benson, M. A. et al. Ryanodine receptors are part of the myospryn complex in cardiac muscle. *Sci. Rep.* **7**, 6312 (2017).
14. Wang, D., Tai, P. W. L. & Gao, G. Adeno-associated virus vector as a platform for gene therapy delivery. *Nat. Rev. Drug Discov.* **18**, 358–378 (2019).
15. Reynolds, J. G., McCalmon, S. A., Tomczyk, T. & Naya, F. J. Identification and mapping of protein kinase A binding sites in the costameric protein myospryn. *Biochim. Biophys. Acta* **1773**, 891–902 (2007).
16. Sarparanta, J. et al. Interactions with M-band titin and calpain 3 link myospryn (CMYA5) to tibial and limb-girdle muscular dystrophies. *J. Biol. Chem.* **285**, 30304–30315 (2010).
17. Yang, X. et al. Tri-iodo-l-thyronine promotes the maturation of human cardiomyocytes-derived from induced pluripotent stem cells. *J. Mol. Cell. Cardiol.* **72**, 296–304 (2014).
18. Rog-Zielinska, E. A. et al. Glucocorticoids promote structural and functional maturation of foetal cardiomyocytes: a role for PGC-1α. *Cell Death Differ.* **22**, 1106–1116 (2015).
19. Parikh, S. S. et al. Thyroid and glucocorticoid hormones promote functional T-tubule development in human-induced pluripotent stem cell-derived cardiomyocytes. *Circ. Res.* **121**, 1323–1330 (2017).
20. Feaster, T. K. et al. Matrigel mattress: a method for the generation of single contracting human-induced pluripotent stem cell-derived cardiomyocytes. *Circ. Res.* **117**, 995–1000 (2015).
21. Ronaldson-Bouchard, K. et al. Advanced maturation of human cardiac tissue grown from pluripotent stem cells. *Nature* **556**, 239–243 (2018).
22. Li, L. et al. Generation of high-performance human cardiomyocytes and engineered heart tissues from extended pluripotent stem cells. *Cell Discov.* **8**, 105 (2022).
23. Zhang, D. et al. Tissue-engineered cardiac patch for advanced functional maturation of human ESC-derived cardiomyocytes. *Biomaterials* **34**, 5813–5820 (2013).
24. Weinberger, F., Mannhardt, I. & Eschenhagen, T. Engineering cardiac muscle tissue: a maturating field of research. *Circ. Res.* **120**, 1487–1500 (2017).
25. Huebsch, N. et al. Metabolically driven maturation of human-induced-pluripotent-stem-cell-derived cardiac microtissues on microfluidic chips. *Nat. Biomed. Eng.* **6**, 372–388 (2022).
26. Wang, G. et al. Modeling the mitochondrial cardiomyopathy of Barth syndrome with induced pluripotent stem cell and heart-on-chip technologies. *Nat. Med.* **20**, 616–623 (2014).
27. Pasqualini, F. S. et al. Structural phenotyping of stem cell-derived cardiomyocytes. *Stem Cell Reports* **4**, 340–347 (2015).
28. Bray, M. A., Sheehy, S. P. & Parker, K. K. Sarcomere alignment is regulated by myocyte shape. *Cell Motil. Cytoskeleton* **65**, 641–651 (2008).
29. Gerdes, A. M. & Capasso, J. M. Structural remodeling and mechanical dysfunction of cardiac myocytes in heart failure. *J. Mol. Cell. Cardiol.* **27**, 849–856 (1995).
30. Eisner, D. A., Caldwell, J. L., Kistamás, K. & Trafford, A. W. Calcium and excitation–contraction coupling in the heart. *Circ. Res.* **121**, 181–195 (2017).
31. Hong, T.-T. et al. BIN1 is reduced and Cav1.2 trafficking is impaired in human failing cardiomyocytes. *Heart Rhythm* **9**, 812–820 (2012).
32. Guo, A. et al. E-C coupling structural protein junctophilin-2 encodes a stress-adaptive transcription regulator. *Science* **362**, eaan3303 (2018).
33. Guo, A. et al. Overexpression of junctophilin-2 does not enhance baseline function but attenuates heart failure development after cardiac stress. *Proc. Natl Acad. Sci. USA* **111**, 12240–12245 (2014).
34. Liu, Y. et al. In mice subjected to chronic stress, exogenous cBIN1 preserves calcium-handling machinery and cardiac function. *JACC Basic Transl. Sci.* **5**, 561–578 (2020).
35. Feyen, D. A. M. et al. Metabolic maturation media improve physiological function of human iPSC-derived cardiomyocytes. *Cell Rep.* **32**, 107925 (2020).
36. Hiess, F. et al. Distribution and function of cardiac ryanodine receptor clusters in live ventricular myocytes. *J. Biol. Chem.* **290**, 20477–20487 (2015).
37. Chen, C. Y. et al. Suppression of detyrosinated microtubules improves cardiomyocyte function in human heart failure. *Nat. Med.* **24**, 1225–1233 (2018).
38. Tarnavski, O. et al. Mouse cardiac surgery: comprehensive techniques for the generation of mouse models of human diseases and their application for genomic studies. *Physiol. Genomics* **16**, 349–360 (2004).
39. Durham, J. T. et al. Myospryn is a direct transcriptional target for MEF2A that encodes a striated muscle, α-actinin-interacting, costamere-localized protein. *J. Biol. Chem.* **281**, 6841–6849 (2006).
40. Lin, Z. et al. Cardiac-specific YAP activation improves cardiac function and survival in an experimental murine MI model. *Circ. Res.* **115**, 354–363 (2014).
41. Wang, S., Guo, Y. & Pu, W. T. AAV gene transfer to the heart. *Methods Mol. Biol.* **2158**, 269–280 (2021).
42. Chen, B., Zhang, C., Guo, A. & Song, L.-S. In situ single photon confocal imaging of cardiomyocyte T-tubule system from Langendorff-perfused hearts. *Front. Physiol.* **6**, 134 (2015).
43. Shang, W. et al. Imaging $Ca^{2+}$ nanosparks in heart with a new targeted biosensor. *Circ. Res.* **114**, 412–420 (2014).
44. Akerberg, A. A. et al. RBPMS2 is a myocardial-enriched splicing regulator required for cardiac function. *Circ. Res.* **131**, 980–1000 (2022).
45. Liu, X. et al. Increased reactive oxygen species-mediated $Ca^{2+}$/calmodulin-dependent protein kinase II activation contributes to calcium handling abnormalities and impaired contraction in Barth syndrome. *Circulation* **143**, 1894–1911 (2021).
46. Zhou, P. et al. Dynamic changes in P300 enhancers and enhancer-promoter contacts control mouse cardiomyocyte maturation. *Dev. Cell* **58**, 898–914.e7 (2023).
47. Lu, F. et al. Imaging sarcoplasmic reticulum $Ca^{2+}$ signaling in intact cardiac myocytes. *Circulation* **142**, 1503–1505 (2020).
48. Lu, F. and Pu, W. T. Code for analysis of Ca2+, RYR2, and T-tubule imaging data. *Zenodo* https://doi.org/10.5281/zenodo.13366870 (2024).


## Acknowledgements

We thank the Gift of Life Donor Program of Philadelphia for enabling the procurement of human hearts from deceased organ donors; W. Chen, University of Calgary, for providing us with the *Ryr2-gfp* mouse line; J. Milosh for coverslip preparation; and M. Rosnach for cell-patterning artwork. F.L. discloses support for the research described in this study from Fudan University (JIH1340085Y) and the American Heart Association (20POST35200233); W.T.P. discloses support for the research described in this study from the National Institutes of Health (R01HL163937, R01HL146634 and UH3TR003279). K.K.P. discloses support for the research described in this study from the National Institutes of Health (UH3TR003279). K.B.M. discloses support for the research described in this study from the National Institutes of Health (R01HL149891 and R01HL105993).

## Author contributions

F.L. and W.T.P. conceptualized the project. F.L., W.X., M.A.T., K.S., K.K.P., D.Z. and W.T.P. developed the methodology. F.L., C.L., Q.M., Z.W., R.H.B., M.P., P.B., B.X., Y.X., S.X., X.Z. and A.P. conducted investigations. F.J.N., K.C.B. and K.B.M. produced materials and reagents. W.T.P., K.K.P. and K.B.M. acquired funding. W.T.P., K.K.P. and K.B.M. administered the project. F.L. wrote the original draft. F.L. and W.T.P. reviewed and edited the manuscript.

## Competing interests

K.B.M. holds research grants from Amgen and serves as a scientific consultant/advisory board member for Bristol Myers Squibb. W.T.P. and F.L. have filed for intellectual property rights on miniCMYA5. All other authors declare no competing interests.

## Additional information

**Extended data** is available for this paper at https://doi.org/10.1038/s41551-024-01253-z.

**Supplementary information** The online version contains supplementary material available at https://doi.org/10.1038/s41551-024-01253-z.

**Correspondence and requests for materials** should be addressed to Fujian Lu or William T. Pu.

**Peer review information** *Nature Biomedical Engineering* thanks Bjorn Knollmann and the other, anonymous, reviewer(s) for their contribution to the peer review of this work. Peer reviewer reports are available.

https://doi.org/10.1038/s41551-024-01253-z

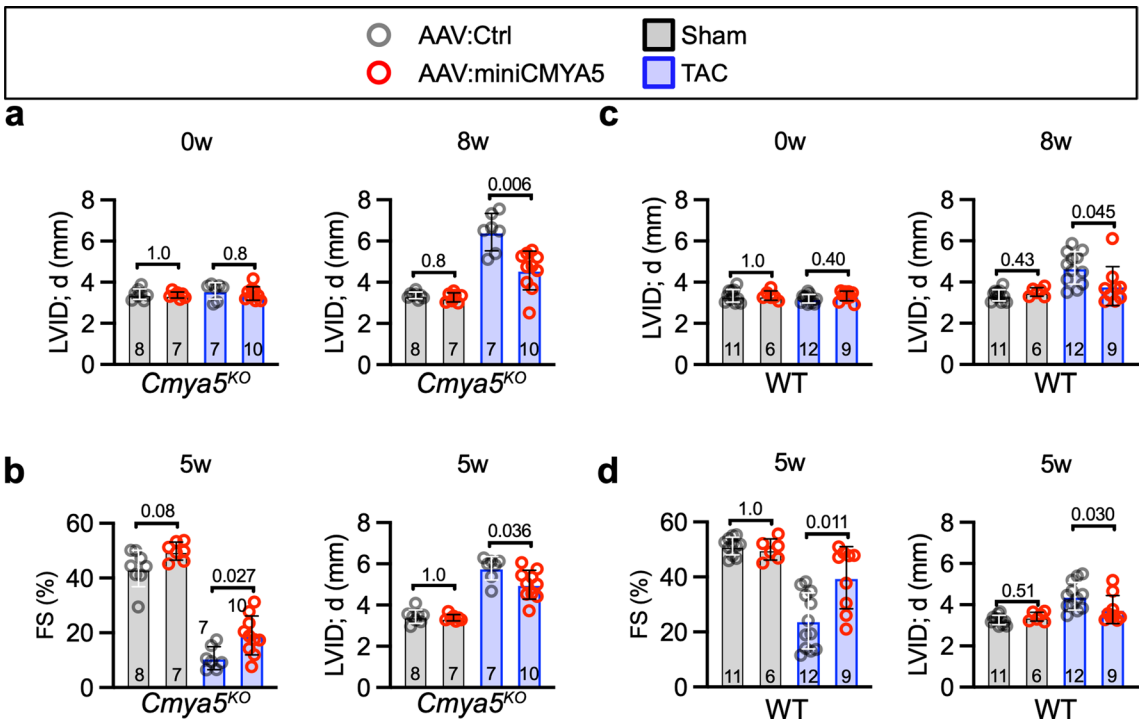


**Extended Data Fig. 1 | Echocardiographic analysis of AAV-miniCMYA5 treatment in a murine pressure-overload model. a**–**d**, *Cmya5*$^{KO}$ (**a** and **b**) or WT (**c** and **d**) mice were treated with AAV-Ctrl or AAV-miniCMYA5 and then Sham or TAC surgery. Left ventricular internal diameter at end-diastole (LVID;d, **a** and **c**) or fractional shortening (FS, **b** and **d**) were measured at the indicated time point. Mann Whitney test with Bonferroni correction for 2 comparisons. Data are shown as mean ± SD.

https://doi.org/10.1038/s41551-024-01253-z

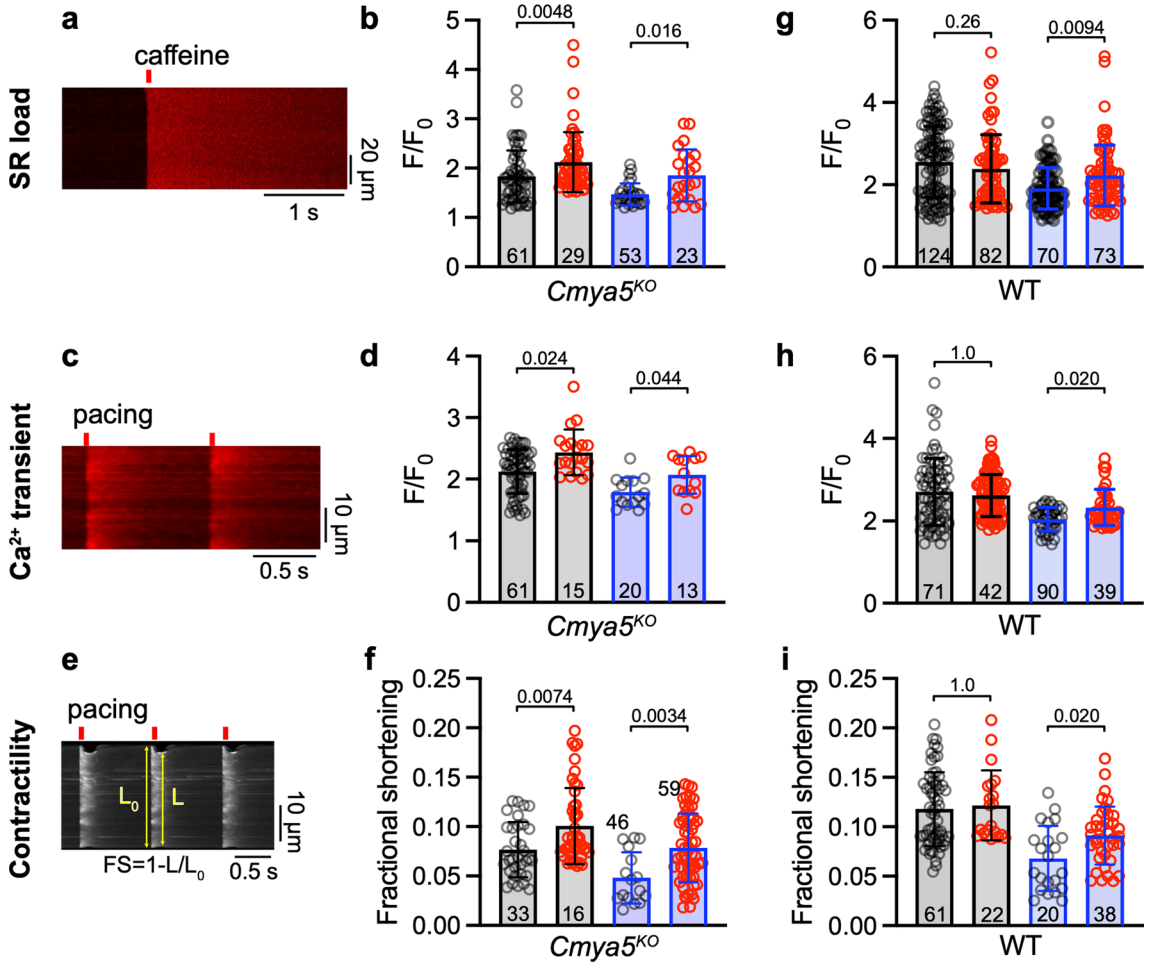


**Extended Data Fig. 2 | Assessment of contractility, $Ca^{2+}$ transient, and SR load in dissociated murine cardiomyocytes.** *Cmya5*$^{KO}$ or WT mice were treated with AAV-GFP or AAV-miniCMYA5 following the timeline shown in Fig. 3a. Cardiomyocytes were dissociated from mouse hearts, loaded with $Ca^{2+}$-sensitive dye Rhod2, and analyzed by confocal line scan imaging during 1 Hz pacing. **a-f**, *Cmya5*$^{KO}$. **g-i**, WT. Representative confocal line scan images are shown in **a**, **c**, and **e**. SR load was measured as the peak fluorescent intensity after cells were treated with caffeine (SR load $F/F_0$, **b** and **g**). $Ca^{2+}$ transient amplitude was determined from the peak fluorescent intensity divided by the baseline intensity ($Ca^{2+}$ transient $F/F_0$, **d** and **h**). Contractility was measured as the fractional shortening of the cardiomyocyte (Fractional shortening: **f** and **i**). Mann-Whitney with Bonferonni correction for two tests. Data are shown as mean ± SD.

https://doi.org/10.1038/s41551-024-01253-z

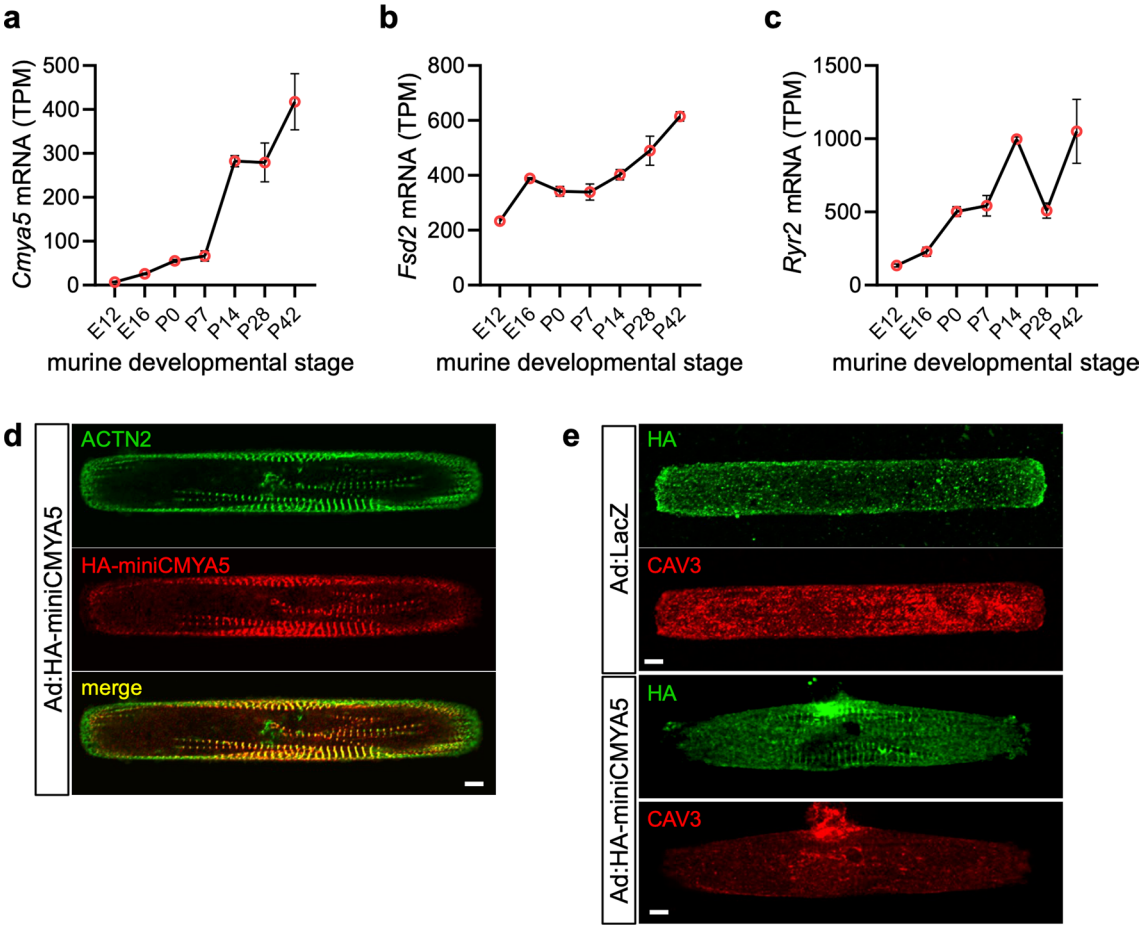


**Extended Data Fig. 3 | Expression and localization of CMYA5 in hiPSC-CMs and murine cardiomyocytes. a-c.** Expression of *Cmya5*, *Fsd2*, and *Ryr2* mRNAs during murine heart development. Gene expression was measured in purified ventricular cardiomyocytes at the indicated stage by RNA-seq. Data are from GSE195902. n = 3 per time point. **d.** Co-localization of miniCMYA5 with ACTN2 in patterned hiPSC-CMs. **e.** Increased organization of RYR2/jSR induced by miniCMYA5 in hiPSC-CMs was not sufficient to stimulate detectable formation of T-tubules, marked by CAV3. Bar = 5 µm. Data are shown as mean ± SD.

https://doi.org/10.1038/s41551-024-01253-z

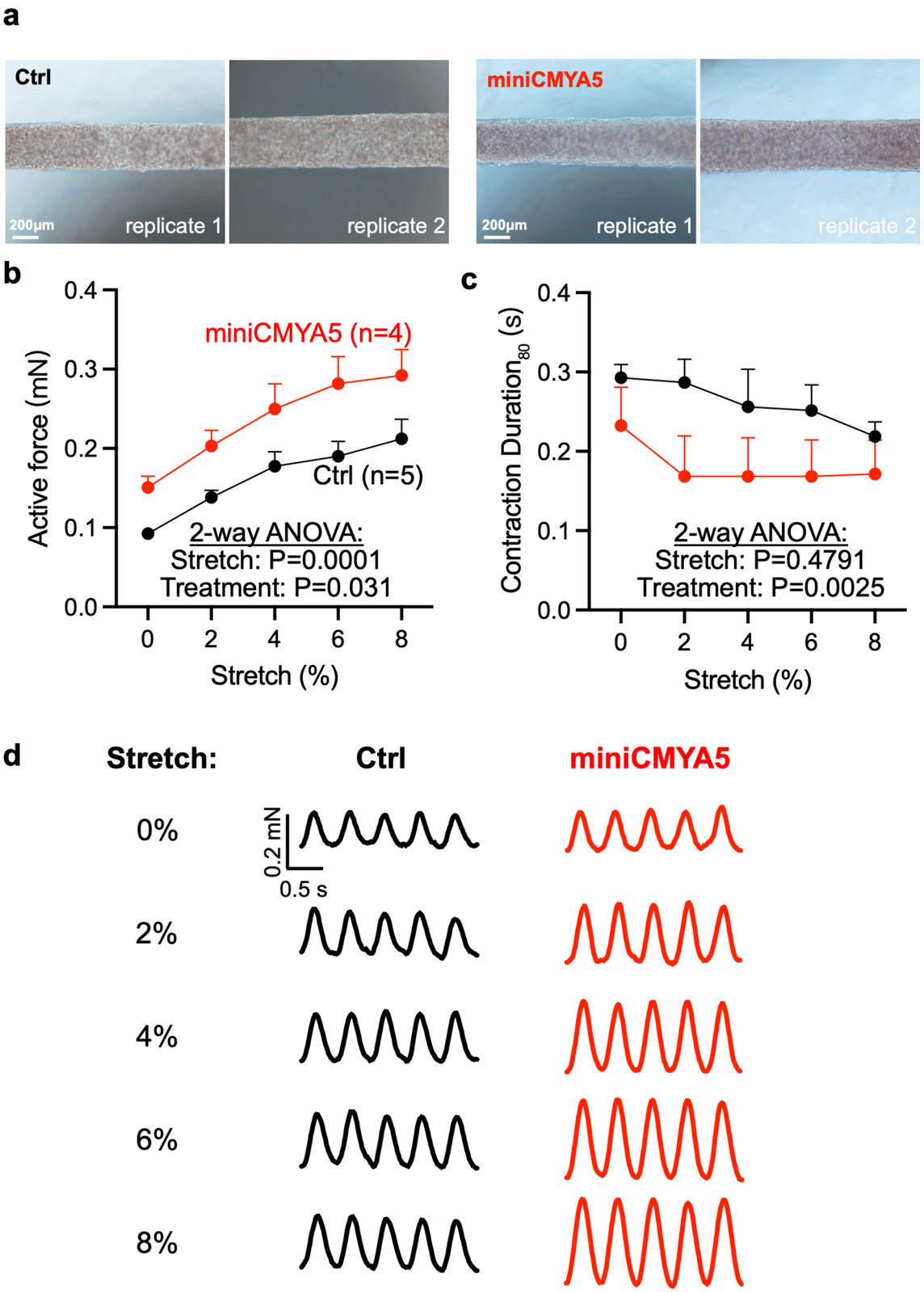


**Extended Data Fig. 4 | MiniCMYA5 enhanced excitation-contraction coupling and force generation by hiPSC-CMs. a**. Representative images of engineered heart tissues (EHTs) generated from hiPSC-CMs treated with Ad:GFP (Ctrl) or Ad:miniCMYA5. EHTs were electrically paced at 2 Hz. **b**. Active force produced by EHTs as a function of passive stretch above the resting length. **c**. Contraction duration of EHTs as a function of passive stretch. The contraction duration was measured at 80% maximal force. **d**. Representative traces of EHT active force over time as a function of initial stretch. Data are shown as mean ± SD.

nature portfolio

Corresponding author(s): William Pu and Fujian Lu

Last updated by author(s): Jun 8, 2024

# Reporting Summary

Nature Portfolio wishes to improve the reproducibility of the work that we publish. This form provides structure for consistency and transparency in reporting. For further information on Nature Portfolio policies, see our Editorial Policies and the Editorial Policy Checklist.

## Statistics

For all statistical analyses, confirm that the following items are present in the figure legend, table legend, main text, or Methods section.

| n/a | Confirmed | |
|---|---|---|
| ☐ | ☒ | The exact sample size (*n*) for each experimental group/condition, given as a discrete number and unit of measurement |
| ☐ | ☒ | A statement on whether measurements were taken from distinct samples or whether the same sample was measured repeatedly |
| ☐ | ☒ | The statistical test(s) used AND whether they are one- or two-sided<br>*Only common tests should be described solely by name; describe more complex techniques in the Methods section.* |
| ☒ | ☐ | A description of all covariates tested |
| ☐ | ☒ | A description of any assumptions or corrections, such as tests of normality and adjustment for multiple comparisons |
| ☐ | ☒ | A full description of the statistical parameters including central tendency (e.g. means) or other basic estimates (e.g. regression coefficient) AND variation (e.g. standard deviation) or associated estimates of uncertainty (e.g. confidence intervals) |
| ☐ | ☒ | For null hypothesis testing, the test statistic (e.g. *F*, *t*, *r*) with confidence intervals, effect sizes, degrees of freedom and *P* value noted<br>*Give P values as exact values whenever suitable.* |
| ☒ | ☐ | For Bayesian analysis, information on the choice of priors and Markov chain Monte Carlo settings |
| ☒ | ☐ | For hierarchical and complex designs, identification of the appropriate level for tests and full reporting of outcomes |
| ☒ | ☐ | Estimates of effect sizes (e.g. Cohen's *d*, Pearson's *r*), indicating how they were calculated |

*Our web collection on statistics for biologists contains articles on many of the points above.*

## Software and code

Policy information about availability of computer code

| | |
|---|---|
| Data collection | VisualSonics Vevo 2100 for echocardiogram, Olympus FV3000 confocal microscope for imaging |
| Data analysis | Graphpad Prism 10, Fiji (ImageJ 1.51w), Interactive Data Language 7.1. Custom code is provided as Supplementary Information and is also available at https://github.com/pulab/miniCMYA5_Ca_analysis. |

For manuscripts utilizing custom algorithms or software that are central to the research but not yet described in published literature, software must be made available to editors and reviewers. We strongly encourage code deposition in a community repository (e.g. GitHub). See the Nature Portfolio guidelines for submitting code & software for further information.

## Data

Policy information about availability of data

All manuscripts must include a data availability statement. This statement should provide the following information, where applicable:

- Accession codes, unique identifiers, or web links for publicly available datasets
- A description of any restrictions on data availability
- For clinical datasets or third party data, please ensure that the statement adheres to our policy

The data supporting the results in this study are available within the paper and its Supplementary Information. Source data are provided with this paper. The raw and analysed datasets generated during the study are available for research purposes from the corresponding authors on reasonable request.

## Research involving human participants, their data, or biological material

Policy information about studies with human participants or human data. See also policy information about sex, gender (identity/presentation), and sexual orientation and race, ethnicity and racism.

| | |
|---|---|
| Reporting on sex and gender | Please see Supplementary Table 1. |
| Reporting on race, ethnicity, or other socially relevant groupings | Please see Supplementary Table 1. |
| Population characteristics | Supplementary Table 1 reports age, sex, BMI, LV Mass Index, LVEF, and history of diabetes, hypertension, b-blocker usage, and ACE inhibitor usage. |
| Recruitment | Explanted hearts (diseased hearts, or unused donor hearts) were used for this study. |
| Ethics oversight | Institutional Review Boards at the University of Pennsylvania and the Gift-of-Life Donor Program (Pennsylvania, USA). |

Note that full information on the approval of the study protocol must also be provided in the manuscript.

# Field-specific reporting

Please select the one below that is the best fit for your research. If you are not sure, read the appropriate sections before making your selection.

☒ Life sciences ☐ Behavioural & social sciences ☐ Ecological, evolutionary & environmental sciences

For a reference copy of the document with all sections, see nature.com/documents/nr-reporting-summary-flat.pdf

# Life sciences study design

All studies must disclose on these points even when the disclosure is negative.

| | |
|---|---|
| Sample size | Power calculations were performed for physiological measurements of organ function. Sample sizes exceeded the number of samples determined by power calculations, which were based on biologically meaningful effect size and on our historical standard deviations. |
| Data exclusions | No data were excluded from analysis. For live cardiomyocyte imaging, round globular cells were not studied, as cells with this morphology are damaged or dying. |
| Replication | Biological-replication information is provided in the figure captions. |
| Randomization | Samples were randomly allocated. |
| Blinding | The investigators were blinded to group allocation during data acquisition and analysis. |

# Reporting for specific materials, systems and methods

We require information from authors about some types of materials, experimental systems and methods used in many studies. Here, indicate whether each material, system or method listed is relevant to your study. If you are not sure if a list item applies to your research, read the appropriate section before selecting a response.

### Materials & experimental systems

| n/a | Involved in the study |
|---|---|
| ☐ | ☒ Antibodies |
| ☐ | ☒ Eukaryotic cell lines |
| ☒ | ☐ Palaeontology and archaeology |
| ☐ | ☒ Animals and other organisms |
| ☒ | ☐ Clinical data |
| ☒ | ☐ Dual use research of concern |
| ☒ | ☐ Plants |

### Methods

| n/a | Involved in the study |
|---|---|
| ☒ | ☐ ChIP-seq |
| ☒ | ☐ Flow cytometry |
| ☒ | ☐ MRI-based neuroimaging |

## Antibodies

| | |
|---|---|
| Antibodies used | Information for the antibodies used are provided in supplemental tables.<br>CMYA5 Dr. Francisco J. Naya, Boston University Rabbit 1:500 (WB) 1:100(IF) |

CMYA5 Life Technologies PA5140296 Rabbit 1:500 (WB) 1:100 (IF)
CMYA5 Homemade Rabbit 1:300 (WB)
RYR2 Sigma-Aldrich R128 Mouse 1:500 (WB) 1:100 (IF)
CAV3 Life Technologies PA1066 Rabbit 1:100 (IF)
FSD2 Santa Cruz Biotechnology sc-393072 Mouse 1:500 (WB) 1:100 (IF)
SAA Sigma-Aldrich A7811 Mouse 1:100 (IF)
GAPDH Proteintech 60004-1-Ig Mouse 1:500 (WB)
HA tag Cell Signaling Technology 3724S Rabbit 1:100 (IF)
Streptavidin-Horseradish Peroxidase (HRP) Conjugate Invitrogen SA10001 1:3000 (WB)

Validation

CMYA5 antibody -validated by multiple papers: 1(IF), 2(WB)
CMYA5 antibody -validated by coIP and negative control in this paper (IF, WB)
CMYA5 antibody -validated by CMYA5 KO heart lysates in this paper (WB)
RYR2 antibody -validated by multiple papers: 3(IF) 4(IF) 5(WB)
CAV3 antibody -validated by multiple papers: 6(IF) 7(IF)
FSD2 antibody -validated by Santa Cruz Biotechnology: 8 (IF, WB)
SAA antibody -validated by multiple papers: 9(IF) 10(IF)
GAPDH antibody -validated by paper: 11 (WB)
HA tag antibody -validated by multiple papers 8 (IF) 12(IF) 13(IF) and negative control in this paper (IF, WB)
Streptavidin-Horseradish Peroxidase (HRP) Conjugate antibody -validated by multiple papers: 14(WB) 15(WB)
Citations
1. Durham, J. T. et al. Myospryn Is a Direct Transcriptional Target for MEF2A That Encodes a Striated Muscle, "-Actinin-interacting, Costamere-localized Protein*. J. Biol. Chem. 281, 6841–6849 (2006).
2. Kielbasa, O. M. et al. Myospryn is a calcineurin-interacting protein that negatively modulates slow-fiber-type transformation and skeletal muscle regeneration. FASEB J. 25, 2276–2286 (2011).
3. Shang, W. et al. Imaging Ca2+ nanosparks in heart with a new targeted biosensor. Circ. Res. 114, 412–420 (2014).
4. Sahu, G. et al. Junctophilin Proteins Tether a Cav1-RyR2-KCa3.1 Tripartite Complex to Regulate Neuronal Excitability. Cell Rep. 28, 2427–2442.e6 (2019).
5. Vaithianathan, T. et al. Subtype identification and functional characterization of ryanodine receptors in rat cerebral artery myocytes. American Journal of Physiology-Cell Physiology vol. 299 C264–C278 (2010).
6. Guo, Y. et al. Hierarchical and stage-specific regulation of murine cardiomyocyte maturation by serum response factor. Nat. Commun. 9, 3837 (2018).
7. VanDusen, N. J. et al. Massively parallel in vivo CRISPR screening identifies RNF20/40 as epigenetic regulators of cardiomyocyte maturation. Nat. Commun. 12, 4442 (2021).
8. Lu, F., et al. CMYA5 establishes cardiac dyad architecture and positioning. Nat Commun 13, 2185 (2022).
9. Prondzynski, M. et al. Disease modeling of a mutation in "-actinin 2 guides clinical therapy in hypertrophic cardiomyopathy. EMBO Mol. Med. 11, e11115 (2019).
10. Chen, X. et al. QKI is a critical pre-mRNA alternative splicing regulator of cardiac myofibrillogenesis and contractile function. Nat. Commun. 12, 89 (2021).
11. Leto, D. E. et al. Genome-wide CRISPR Analysis Identifies Substrate-Specific Conjugation Modules in ER-Associated Degradation. Mol. Cell 73, 377–389.e11 (2019).
12. Tunc-Ozcan, E. et al. Activating newborn neurons suppresses depression and anxiety-like behaviors. Nat. Commun. 10, 3768 (2019).
13. Chai, Q. et al. A Mycobacterium tuberculosis surface protein recruits ubiquitin to trigger host xenophagy. Nature Communications vol. 10 (2019).
14. Yap, K., Chung, T. H. & Makeyev, E. V. Hybridization-proximity labeling reveals spatially ordered interactions of nuclear RNA compartments. Molecular Cell vol. 82 463-478.e11 (2022).
15. Cardamone, M. D. et al. Neuralized-like protein 4 (NEURL4) mediates ADP-ribosylation of mitochondrial proteins. J. Cell Biol. 221, (2022).

## Eukaryotic cell lines

Policy information about cell lines and Sex and Gender in Research

| | |
|---|---|
| Cell line source(s) | HEK293T cells (human, ATCC, CRL-3216 & CRL-1573) for virus production. |
| Authentication | Cell lines are authenticated by ATCC via STR profiling. |
| Mycoplasma contamination | The cell line tested negative for mycoplasma. |
| Commonly misidentified lines (See ICLAC register) | No commonly misidentified cell lines were used. |

## Animals and other research organisms

Policy information about studies involving animals; ARRIVE guidelines recommended for reporting animal research, and Sex and Gender in Research

| | |
|---|---|
| Laboratory animals | Mice, mixed strains, ages P1 to 6 months, male and female. Cmya5Δ/Δ (C57BL/6NJ-Cmya5em1(IMPC)J/Mmja; Stock no. 032826, Jackson Laboratory); Ryr2-GFP knockin (129sve, gift from Dr. Wayne Chen, University of Calgary). Descriptions of the mice used for the experiments can be found in the relevant figure captions and in Methods. All animal experiments were performed under protocols approved by the Boston Children's Hospital Institutional Animal Care and Use Committee. |

| | |
|---|---|
| Wild animals | The study did not involve wild animals. |
| Reporting on sex | Both male and female mice were used. |
| Field-collected samples | The study did not involve samples collected from the field. |
| Ethics oversight | Boston Children's Hospital (BCH) Institutional Animal Care and Use Committee (IACUC). |

Note that full information on the approval of the study protocol must also be provided in the manuscript.